Journal of Physics D: Applied Physics

TOPICAL REVIEW

Interband cascade lasers

Interband Cascade Lasers

Journal:	*Journal of Physics D: Applied Physics*
Manuscript ID:	JPhysD-104332.R1
Manuscript Type:	Topical Review
Date Submitted by the Author:	21-Jan-2015
Complete List of Authors:	Vurgaftman, Igor; Naval Research Laboratory, Code 5613 Weih, Robert; University of Wuerzburg, Kamp, Martin; University of Wuerzburg, Meyer, Jerry; Naval Research Laboratory, Canedy, Chadwick; Naval Research Laboratory, Kim, Chul Soo; Naval Research Laboratory, Kim, Mijin; Sotera Defense Solutions, Bewley, William; Naval Research Laboratory, Merritt, Charles; Naval Research Laboratory, Abell, Joshua; Naval Research Laboratory, Hoefling, Sven; University of St. Andrews,
Article Keywords:	mid-infrared lasers, semiconductor lasers, interband cascade lasers
Abstract:	We review the current status of interband cascade lasers (ICLs) emitting in the midwave infrared. The ICL may be considered the hybrid of a conventional diode laser that generates photons via electron-hole recombination, and an intersubband-based quantum cascade laser (QCL) that stacks multiple stages for enhanced current efficiency. Following a brief historical overview, we discuss theoretical aspects of the active region and core designs, growth by molecular beam epitaxy, and the processing of broad-area, narrow-ridge, and distributed-feedback (DFB) devices. We then review the experimental performance of pulsed broad area ICLs, as well as the cw characteristics of narrow ridges having good beam quality and DFBs producing output in a single spectral mode. Because the threshold drive powers are far lower than those of QCLs throughout the λ = 3-6 μm spectral band, ICLs are increasingly viewed as the laser of choice for mid-IR laser spectroscopy applications that do not require high output power but need to be hand-portable and/or battery operated. Demonstrated ICL performance characteristics to date include threshold current densities as low as 106 A/cm2 at room temperature (RT), continuous-wave (cw) threshold drive powers as low as 29 mW at RT, maximum cw operating temperatures as high as 118 °C, maximum cw output powers exceeding 400 mW at RT, maximum cw wallplug efficiencies as high as 18% at RT, maximum cw single-mode output powers as high as 55 mW at RT, and single-mode output at λ = 5.2 μm with a cw drive power of only 138 mW at RT.

Interband Cascade Lasers

I. Vurgaftman,[a] R. Weih,[c] M. Kamp,[c] J. R. Meyer,[a] C. L. Canedy,[a] C. S. Kim,[a] M. Kim,[d]
W. W. Bewley,[a] C. D. Merritt,[a] J. Abell,[a] and S. Höfling[b,c]

[a]*Naval Research Laboratory, Code 5613, Washington DC 20375, USA*
[b]*University of St Andrews, School of Physics and Astronomy, St Andrews, Fife KY16 9SS, UK*
[c]*Universität Würzburg, Technische Physik, Am Hubland, D-97074 Würzburg, Germany*
[d]*Sotera Defense Solutions, Inc., 7230 Lee DeForest Drive, Suite 100, Columbia MD 21046, USA*

Abstract

We review the current status of interband cascade lasers (ICLs) emitting in the midwave infrared. The ICL may be considered the hybrid of a conventional diode laser that generates photons via electron-hole recombination, and an intersubband-based quantum cascade laser (QCL) that stacks multiple stages for enhanced current efficiency. Following a brief historical overview, we discuss theoretical aspects of the active region and core designs, growth by molecular beam epitaxy, and the processing of broad-area, narrow-ridge, and distributed-feedback (DFB) devices. We then review the experimental performance of pulsed broad area ICLs, as well as the cw characteristics of narrow ridges having good beam quality and DFBs producing output in a single spectral mode. Because the threshold drive powers are far lower than those of QCLs throughout the λ = 3-6 μm spectral band, ICLs are increasingly viewed as the laser of choice for mid-IR laser spectroscopy applications that do not require high output power but need to be hand-portable and/or battery operated. Demonstrated ICL performance characteristics to date include threshold current densities as low as 106 A/cm^2 at room temperature (RT), continuous-wave (cw) threshold drive powers as low as 29 mW at RT, maximum cw operating temperatures as high as 118 °C, maximum cw output powers exceeding 400 mW at RT, maximum cw wallplug efficiencies as high as 18% at RT, maximum cw single-mode output powers as high as 55 mW at RT, and single-mode output at λ = 5.2 μm with a cw drive power of only 138 mW at RT.

1. Introduction and historical background

The interband cascade laser (ICL) is a promising mid-IR (defined here as λ = 3-6 μm) source that combines the relatively long upper-level recombination lifetime of a conventional diode laser with the voltage-efficient cascading scheme introduced by the quantum cascade laser (QCL, which produces coherent light via intersubband transitions within the conduction band). The mid-IR spectral region has gained increasing relevance in recent years, because it hosts numerous "fingerprint" spectral lines that can be used to sense trace gases such as methane, carbon dioxide, carbon monoxide, formaldehyde, *etc*. While practical sensing systems typically require cw emission into a single spectral mode, a low output power on the order of 1 mW is usually sufficient [1]. On the other hand, such military applications as infrared countermeasures require substantial cw output powers, whereas spectral purity is generally less critical. Other potential applications for compact and efficient mid-IR sources include industrial process control, clinical breath analysis, free-space optical communications, IR scene projection, and the detection of chemical/biological threats.

Nonetheless, until 2002 no semiconductor source could offer the continuous-wave (cw) operation at ambient temperature [2] that is essential if any mid-IR technology is to be considered sufficiently practical for widespread implementation. Earlier development efforts had focused on extending the well-established diode laser architecture, with type-I alignment of the conduction and valence bands [3,4], beyond the 2-3 μm spectral window by increasing the strain in GaSb-based multiple quantum wells (MQWs). However, significant challenges included rapid wavelength scalings of the Auger non-radiative decay and free-carrier absorption loss, carrier escape associated with a marginal valence-band offset in the MQWs, and the general immaturity of GaSb-based growth and processing technologies.

This view was upended by the rapid progress of QCLs grown on InP [5,6]. A modest temperature sensitivity, coupled with efficient heat dissipation, have enabled QCL output powers to reach 5 W cw in a near-diffraction-limited beam at room temperature (RT) [7]. The primary disadvantages are the QCL's high threshold current density, associated with rapid phonon-assisted depopulation of the upper lasing subband and interface roughness scattering (≈ 1 ps), coupled with a bias of at least ≈ 10 V because 30-50 stages are needed to supply sufficient gain.

Even though the ICL was invented in 1994 [8], the same year that the QCL was first demonstrated experimentally, over the intervening period it has received much less attention and far fewer resources have been devoted to its development. Within 2-3 years, the hole injector was added to the concept [9], along with replacement of the single type-II interface in the active gain region with a "W" configuration that incorporates two InAs electron QWs on both sides of the GaInSb hole QW [10]. The "W" structure has become a standard feature of state-of-the-art ICL designs, even though its advantage is not so clear if the nonradiative recombination rate decreases with electron-hole wavefunction overlap even as the gain increases.

While the first experimental realization of an ICL was reported in 1997 [11], the initial devices operated only at cryogenic temperatures [12,13] due to several design aspects that were far from what is now known to be optimal. In particular, excessive electron injector thicknesses induced high threshold current densities and low external differential quantum efficiencies (EDQEs) per stage. Nevertheless, gradual improvements in both designs and the growth techniques led to steady improvement of the temperature performance, with T_{max} = 250-286 K being reached for pulsed operation in the 1998-2000 time frame [14,15,16]. A significant milestone was the demonstration in 2002 of pulsed operation at RT by an ICL with 18 active stages, even though the threshold current density (J_{th}) exceeded 6 kA/cm^2 [17]. Designs employing the "W" active QW configuration subsequently operated at λ = 3.3 μm with much lower RT J_{th} (≈ 1 kA/cm^2), along with cw lasing to T = 200 K [18].

In 2005, the group at Jet Propulsion Laboratory (JPL) substantially reduced the pulsed RT J_{th} further, to 630 A/cm^2, with only 12 active stages [19]. This eventually led to cw operation up to T_{max} = 264 K [20], which enabled JPL to qualify single-mode distributed-feedback (DFB) ICLs for methane detection on the NASA Mars Curiosity Mission [21].

The first ICLs designed, grown, processed, and characterized at Naval Research Laboratory (NRL) were reported in 2006 [22]. In subsequent NRL designs the number of stages was reduced from 10 to 5 [23], in order to minimize the threshold power density. Simulations had determined that an ICL's gain per unit current density is actually quite high, *e.g.*, much higher than in a QCL that typically requires 30 or more stages to minimize J_{th} at RT. NRL subsequently reported a series of advances in such key performance figures of merit as pulsed J_{th}, P_{th}, and EDQE, at and above RT, by employing a much thinner electron injector and two GaSb QWs in the hole injector. The result was a lower RT threshold current density of 1.15 kA/cm^2 for a 10-stage structure. An epitaxial-side-up narrow ridge from that wafer, with Au electroplating deposited on top for heat dissipation, operated cw to T_{max} = 269 K [24].

In 2008, an NRL ICL emitting at λ = 3.75 μm became the first to operate cw at RT [25]. That milestone was made possible by several additional design modifications, including the introduction of lightly *n*-doped GaSb separate-confinement layers (SCLs) to reduce the waveguide loss, decrease of the *n*-doping in the InAs/AlSb optical cladding layers, and reduction of the number of stages to five. The resulting pulsed J_{th} at RT dropped to ≈ 400 A/cm^2, the lowest threshold reported up to that point.

In the past 6 years, NRL has continued to explore numerous other design modifications [26,27,28]. While some had little or no significant impact on the laser performance, others were quite beneficial to the threshold and efficiency. This applies especially to the "carrier rebalancing" concept that will be discussed in the next Section. In parallel, the University of Würzburg (UWUERZ) and Nanoplus GmbH have reported a variety of valuable recent contributions to the ICL development [29,30]. The next Section will discuss these and other state-of-the-art ICL design concepts in depth. While alternative approaches that are suitable for the longest wavelengths of the mid-IR and beyond are now being explored by Prof. Rui Yang and colleagues at the University of Oklahoma [31,32], RT cw operation has not yet been reported. Those concepts are not further discussed in this review.

Although ICLs have been the subject of several previous review articles [33,34], we provide here an up-to-date description of both the physics of operation and the development status. Section 2 discusses the ICL design principles, and also identifies some ingredients that may still be missing from the current picture. The device fabrication aspects of the ICL technology, including growth and processing methods, are discussed in Section 3. Section 4 reviews the operating characteristics of recent broad area, narrow-ridge, and single-spectral-mode distributed-feedback (DFB) ICLs. We conclude in Section 5 with some thoughts on the future prospects for these devices.

2. Theory

In a conventional diode laser, electrons and holes are injected from opposite sides of a *p*-*n* heterojunction, ideally populating all of the MQWs equally (although pronounced non-uniformities can occur under some circumstances). Therefore, the total threshold current density is given by MJ, where J is the threshold current density per QW, and M is the number of QWs, which implies that the parasitic voltage drop $MJ\rho_s$, where ρ_s is the series resistance-area product, scales with the number of QWs. In the mid-IR, the parasitic drop tends to be relatively more significant compared to the “useful” voltage $\hbar\omega/e$, since the currents are often high, and the photon energy $\hbar\omega$ is smaller than at shorter wavelengths.

Cascading mitigates this inefficiency by providing a practical means for connecting the MQWs “in series”, i.e. with the same current flowing through every stage and each injected carrier traversing every active QW in turn [35]. The parasitic voltage drop then decreases to $J\rho_s$ while the “useful” voltage increases to $M\hbar\omega/e$. Cascading can therefore reduce the net threshold power density considerably, provided the required recycling of carriers from valence to conduction band within each stage does not introduce much additional voltage or current [26,36]. Instead of employing an Esaki or tunnel diode to recycle the carriers [37], the ICL exploits the unusual semimetallic band alignment between the narrow-gap semiconductors InAs and Ga(In)Sb [26]. The ICL architecture thus avoids the appreciable internal optical losses (especially due to free hole absorption) that could potentially occur if every stage incorporated a heavily-doped tunnel junction.

The semimetallic overlap between the conduction subbands in an InAs electron QW and the valence subbands in an adjacent Ga(In)Sb hole QW can be tuned with an applied electric field. Since at RT the conduction band minimum of bulk InAs lies ≈ 0.2 eV below the valence band maximum of GaSb, only a modest amount of quantum confinement is sufficient to open a small energy gap E_i. If we now apply an external field F, the lowest conduction subband is lowered with respect to the highest valence subband to create a semimetallic interface (SMIF), at which electrons populate the InAs QW and holes the Ga(In)Sb QW in quasi-thermal equilibrium. This produces a voltage-dependent band overlap $E_{SM}(V) = F(d_e + d_h) - E_i$, where d_e and d_h are the center-of-mass distances from the SMIF of the electron and hole probability densities. At typical ICL operating voltages, this overlap is ≈ 100 meV. Assuming parabolic bands and a common quasi-Fermi level across the SMIF, the generated electron and hole densities are then: $n = p \approx m_r E_{SM}/\pi\hbar^2$, where $m_r = m_e m_h/(m_e + m_h)$ is the reduced effective mass.

The active core of the ICL is comprised of multiple repeated stages, each of which can be subdivided into: (1) the active QWs; (2) the hole injector; and (3) the electron injector. The active QWs can have a type-II or type-I band alignment. The conduction and valence band profiles in a typical type-II ICL designed for emission at $\lambda = 3.7$ μm are shown in Fig. 1, which includes the "W" active regions for two successive stages. The SMIF is seen to separate the hole injector, comprised of coupled GaSb/AlSb QWs, from the electron injector consisting of coupled InAs/AlSb QWs. The field-dependent band overlap between states in the hole injector and active hole QW on the one hand, and states in the electron injector and active electron QW in the next stage on the other determines the carrier densities throughout the active core. We assume a common quasi-Fermi level (QFL) on both sides of the SMIF, since the carrier transport via direct, phonon-assisted, and other tunneling mechanisms should be quite rapid. The relatively long carrier lifetime in the active QWs (~1 ns) then assures that the QFL is discontinuous across the active region of each stage (E_{Fi}-$E_{Fi+1} \geq \hbar\omega \geq E_g$, with E_{Fi}, the electron QFL in stage i, being equal to the hole QFL in stage i-1).

In the ideal design, the applied bias must separate the QFLs in successive stages (equal to the single-stage voltage drop) enough to simultaneously: (1) produce sufficient optical gain to compensate the photon loss in the cavity, and (2) internally generate a quasi-equilibrium carrier density consistent with the voltage drop (accounting for any extrinsic doping). While the first condition is a property of the active QWs only, the second follows from the design and doping of all the electron and hole QWs on both sides of the SMIF. If, for example, the QWs in the electron injector are thicker than optimal, excess carriers will be generated that induce unnecessary free-carrier absorption. Conversely, if the injector QWs are too thin the threshold voltage will exceed that needed to induce the ideal QFL separation of E_{Fi}-$E_{Fi+1} \approx \hbar\omega$ (or somewhat larger if the loss is very high).

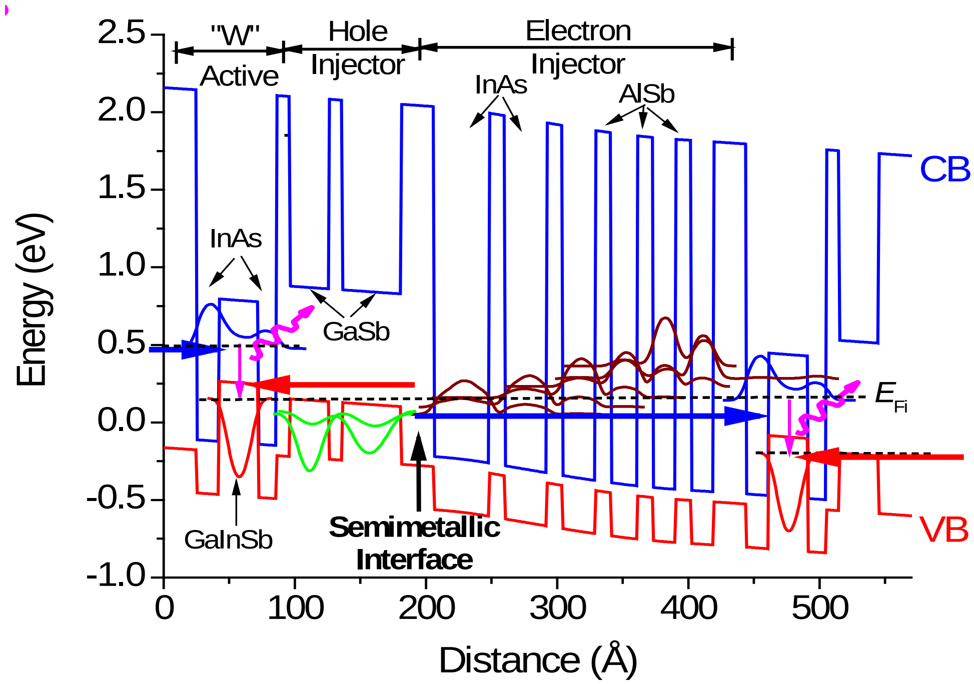

Figure 1. Band diagram of 1.5 stages of a typical ICL active core. Wavefunction probability densities and zone-center energies (indicated by the wavefunction zero points) for some of the most important subbands are superimposed. The probability densities for the active electron (hole) subbands are indicated with blue (red) lines, while those for the injector-electron (hole) subbands are indicated with wine-colored (green) lines. The blue (red) arrows indicate the positions of the quasi-Fermi levels in each stage.

Since many of the states on both sides of the SMIF reside in the injectors rather than the active QWs, only some fraction of the carriers generated internally at the SMIF, or introduced by extrinsic doping, contribute to the optical gain. Therefore, the electron and hole injectors must be carefully designed so as to maximize the fraction of injected carriers populating the active states, while retaining sufficient carrier transport through the injectors to maintain a single QFL throughout the stage.

The current understanding based on extensive empirical testing is that the energy subbands in the two hole injector QWs should lie substantially below the topmost active hole subband, while the states of the thicker electron injector should be located in the vicinity of the SMIF and energetically lower than the active electron QW state. These constraints imply that most of the electrons populating a given stage reside in the injector states rather than the active region, whereas nearly all of the holes transfer successfully to the active hole QW. This is illustrated by the dashed curves in Fig. 2, which plot the electron (wine-colored) and hole (green) densities at threshold for the ICL structure of Fig. 1. The consequence is that if no extrinsic doping is introduced (dashed curves) to supplement the carriers generated at the SMIF, the active hole density will substantially exceed the active electron density at the lasing threshold ($p_{th} >> n_{th}$) [27]. Unless *nnp* (multi-electron) Auger processes strongly dominate the carrier lifetime, the large hole/electron density ratio will tend to reduce the gain per unit current density, and also increase the internal loss unless the cross section for free hole absorption is negligible.

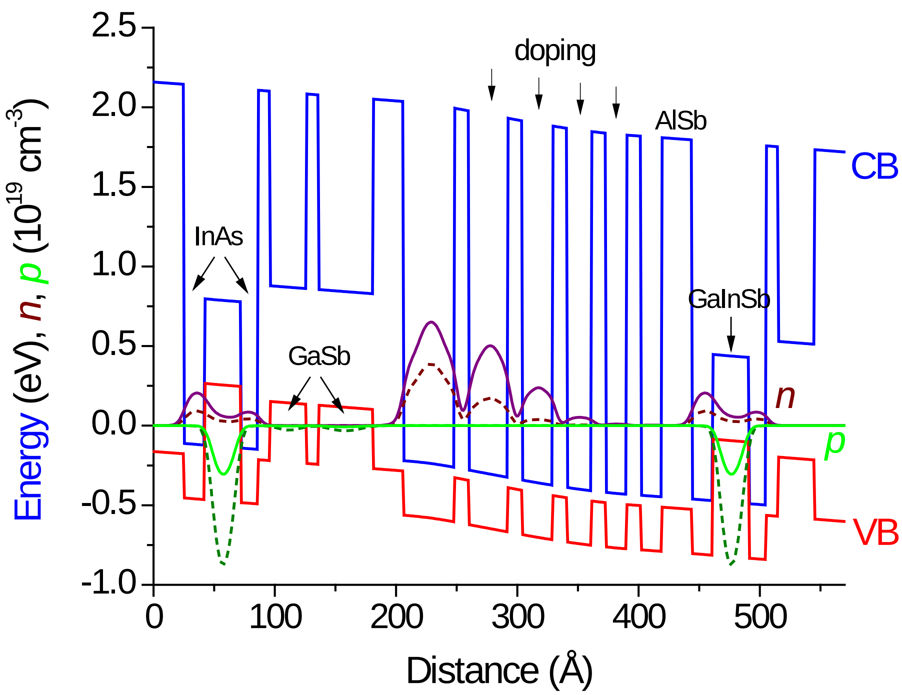

Figure 2. Calculated quasi-equilibrium electron (wine-colored) and hole (green) density distributions for the ICL designs without (dashed) and with (solid) carrier rebalancing. Rebalancing is achieved by increasing the extrinsic Si doping level in four of the InAs electron injector QWs from 4×10^{17} cm^{-3} to 4×10^{18} cm^{-3}. The blue and red lines indicate the conduction- and valence-band bulk band edges, respectively.

To investigate this potential issue, ICL structures emitting at λ = 3.6-3.9 μm were grown with a series of heavy *n*-doping levels in the electron injectors. While many of the additional electrons remained behind in the injector, NRL simulations predicted that a sufficient fraction would be transferred to the active QWs to substantially alter the hole/electron density ratio there (solid curves in Fig. 2). The total sheet doping, n_s, was varied from 4.8×10^{11} to 7.4×10^{12} cm^{-2}, with 2-4 of the injector QWs receiving the additional doping. This study found that J_{th} at RT was minimized at $n_s \approx 5\times10^{12}$ cm^{-2}, which according to the simulations corresponded to n_{th}/p_{th} only slightly larger than unity. Note that the required sheet doping density substantially exceeds n_{th} and p_{th}, due to the inefficient electron transfer from the doped injector. Another conclusion, from the dependence on doping level, is that the *nnp* and *ppn* Auger coefficients most likely have comparable values [27].

Whereas empirical studies showed it advantageous to employ two GaSb QWs (rather than one) in the hole injector, nominally to suppress electron tunneling leakage from the active region to the electron injector, adding still more QWs to the hole injector is unlikely to prove beneficial. Since the thicknesses of the two hole QWs are adjusted so as to roughly align their topmost subbands at the threshold field, those wells become strongly coupled with two closely-spaced subbands. The GaSb QW thicknesses are chosen so as to place the two subbands ≈ 80-100 meV below the maximum in the active hole QW. This empirical rule should ensure very low occupation of the hole injector states in quasi-equilibrium, as illustrated in Fig. 2. The thicknesses of the AlSb barriers separating the active and hole-injector QWs are typically ≈ 10-12 Å, in order to assure unencumbered hole transport. However, somewhat thicker barriers degrade the ICL performance only gradually.

The QW layer thicknesses in the electron injector should be adjusted so as to produce the required threshold carrier densities, n_{th} and p_{th}, when the heavy extrinsic doping is taken into account. In practice, this occurs when the first electron injector QW has a thickness between 40 and 50 Å. The electric field in the active core is then ≈ 70-90 kV/cm at the lasing threshold. The thickness of each subsequent well is reduced (chirped) so as to maintain coupling between adjacent QWs. However, the electron injector subbands do not actually form a miniband with a common energy level and similar occupation probabilities in all the QWs. Figures 1 and 2 indicate that the lower-energy subbands concentrated near the SMIF are more heavily populated than the higher-energy subbands adjacent to the active region of the next stage. This arrangement reduces the density of states (DOS) at lower energies, while still allowing sufficient electron transport from the SMIF to the active electron QWs.

Like the barriers in the hole injector, the AlSb barriers in the electron injector are relatively thin, *e.g.*, 12-14 Å. However, two of the barriers in each stage are much thicker, at 25-30 Å. One separates the electron and hole injectors at the SMIF, in order to minimize parasitic interband absorption across that interface. The other separates the electron injector from the first active electron QW, so as to isolate the active electron subband from the injector states and prevent significant hybridization while still permitting sufficient electron tunneling.

We finally consider the design of the active QWs. It was mentioned above that state-of-the-art ICLs employ the "W" active region, in which two InAs electron wells sandwich a single GaInSb hole well. The strain induced at the typical $Ga_{1-x}In_xSb$ composition of $x \approx 0.35$ approaches the maximum that can be tolerated while maintaining coherent layer growth. Although hole-well thicknesses ranging from 20 to 30 Å have been employed, no significant trends were observed in the experimental laser thresholds or slope efficiencies.

The "W" configuration of the active QWs substantially enhances the electron-hole wavefunction overlap in comparison to that for an InAs/GaInSb QW with a single type-II interface. For example, when $\lambda = 3.2$ μm and the GaInSb thickness is 20 Å in both structures, the square of the overlap peaks at 42% for the "W" structure but only 17% for the single-interface structure. The two InAs QW thicknesses are chosen so as to dial in the laser emission wavelength via quantum confinement, while maintaining roughly equal electron wavefunction probabilities in the two wells.

The goal in designing the optical waveguide is to simultaneously minimize both the internal loss and the material gain required to reach transparency. While the ICL's active core is unique among semiconductor lasers, the waveguide design follows well-known general principles, apart from the beneficial feature compared to standard diode lasers that both cladding layers are *n*-type (with lower free-carrier absorption loss) because the holes are all generated internally. The ICL waveguide is constructed from the following basic building blocks: (1) the active core, (2) the *n*-doped optical claddings, most commonly comprised of InAs/AlSb short-period superlattices (SLs), although lattice-matched bulk alloys such as AlGaAsSb provide an alternative [38]; (3) the lightly *n*-doped GaSb separate-confinement layers (SCLs); and (4) various transition SLs that separate the other three regions from each other, and from the GaSb substrate/buffer and n^+-InAs(Sb) top contact. The transition SLs reduce the parasitic voltages that would be associated with abrupt heterointerfaces between adjacent regions with very different conduction-band offsets.

Figure 3 shows the waveguide intensity profile for the fundamental TE mode in a 7-stage ICL with two 800-nm-thick SCLs (λ = 3.7 μm). The simulation assumes n_a = 3.45 for the active core, n_c = 3.30 for the SL cladding and transition regions, and n_s = 3.78 for GaSb. The largest uncertainty is in the active core's average index, although its effect on the modal index is minor because the mode is dominated by the GaSb SCLs. While a higher core index would imply a larger confinement factor, Γ_a, and more gain per unit current density, cavity-length studies [39] find that theory tends to overestimate the gain. The index for an $AlAs_{0.08}Sb_{0.92}$ cladding is expected to be only slightly lower (by ≈ 0.1) than that of the SL claddings.

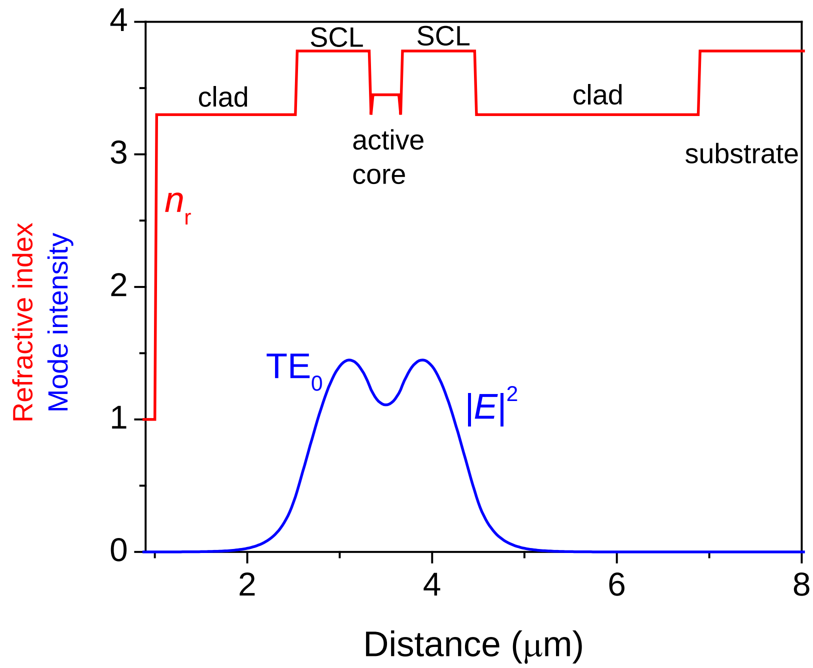

Figure 3. Optical intensity for the fundamental TE mode of a slab ICL waveguide with a 7-stage active core and 800-nm-thick GaSb separate-confinement layers. The refractive indices of the various layers are also shown.

The optical mode overlap with the SCLs is ≈ 77% for the ICL in Fig. 3. In NRL structures, the center of each SCL is *n*-doped at $N_l = 5 \times 10^{15}$ cm^{-3}, whereas 50-nm-thick layers at the edge of each SCL (containing $\Gamma_h \approx 9\%$ of the mode) are doped at $N_h = 1 \times 10^{17}$ cm^{-3} to reduce the voltage drop at the heterointerfaces. Using the data in Ref. 40, the free-carrier contribution to the internal loss from the GaSb SCLs is expected to be ≈ 0.5 cm^{-1} for the structure of Fig. 3.

The clad doping is also non-uniform, in that the inner regions closest to the SCL are doped to $N_i = 7.5 \times 10^{16}$ cm^{-3}, while the outer regions with less mode overlap are doped more heavily, to $N_o = 5 \times 10^{17}$ cm^{-3}. The objective is to trade minimization of the series resistance against minimization of the free-carrier absorption loss. While the total mode overlap with the claddings is estimated to be ≈ 6%, the overlap with the more heavily doped outer regions nearly vanishes. The confinement factor calculated for the active region (including the electron and hole injectors as well as the active QWs) is $\Gamma_a \approx 14\%$. The remainder of the mode (≈ 3%) resides in the InAs/AlSb SL transition regions, which are typically doped to $N_t = 2 \times 10^{17}$ cm^{-3}.

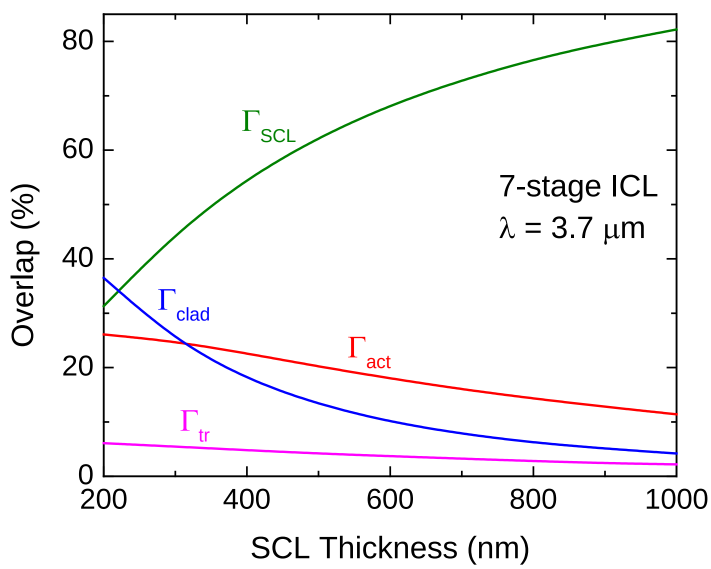

Figure 4. Optical confinement factor for the active core (Γ_{act}), the InAs/AlSb SL cladding layers (Γ_{clad}), the GaSb separate-confinement layers (Γ_{SCL}), and the transition regions (Γ_{tr}).

Figure 4 shows that the optical confinement factors in the active core and cladding layers decrease as the SCL thicknesses increase, as expected. Eventually, the SCLs can become so thick that the TE_2 mode, with two nodes along the growth direction (and an antinode at the active core), can have a greater active-core confinement factor than the TE_0 mode. In state-of-the-art ICLs emitting at $\lambda \approx 4$ μm, the optimal SCL thickness determined by these trade-offs is $t_s \approx 800$ nm.

While the internal loss in the active core is not known precisely, it likely dominates the total loss in state-of-the-art designs. While this suggests it may be beneficial to reduce the active confinement factor Γ_a, eventually the available optical gain becomes insufficient to overcome the losses originating elsewhere in the waveguide. Further studies are needed to fully understand the variation of the internal loss in ICLs with various design parameters. The top cladding layer must be thick enough to minimize mode overlap with the lossy top-contact metallization, while the bottom cladding must be somewhat thicker to avoid mode leakage into the high-index GaSb substrate [41]. These guidelines imply typical top and bottom SL cladding thicknesses of ≈ 1.5 and ≈ 3.0 μm, respectively, for state-of-the-art ICLs emitting at $\lambda = 4$ μm.

3. Technology

a. Growth

ICLs are typically grown on epi-ready Te-doped GaSb wafers in a solid source molecular beam epitaxy (MBE) system equipped with conventional effusion cells for the group-III elements (Al, Ga, In), as well as dopants (Te, Si) and valved cracker cells for the group-V elements (As, Sb). Even though ICLs have been grown using a conventional effusion cell for Sb and an As-cracker operated with a low cracking-zone temperature that primarily provide Sb_4 and As_4 tetramers [42], valved crackers that provide Sb_2 and As_2 reduce the group-V cross incorporation into neighboring layers, and provide adequate flux within the layers grown at different growth rates. In order to provide a smooth surface for the subsequent layers, residual oxides are usually removed thermally in a Sb-rich atmosphere and a GaSb buffer layer is grown.

The low-refractive-index cladding layers, comprised of InAs/AlSb superlattices, are grown next. To avoid reabsorption of the emitted photons, a short period (~ 5 nm) that can be adapted to different emission wavelengths is typically chosen for increasing the effective bandgap by quantum confinement. The typical growth temperature for these cladding layers is in the 400°C to 450°C range. The SL design benefits from the advantageous lattice constant constellation within the 6.1 Å semiconductor family. While the RT lattice constant of InAs (6.0583 Å) is slightly smaller than that of GaSb (6.0959 Å), the lattice constant of AlSb (6.1355 Å) is slightly larger with nearly equal mismatch. Due to the change of both anion and cation at each interface within the InAs/AlSb SL, the interfaces have a significant effect on the morphological, electrical and optical properties [43,44,45]. By introducing so-called soak times, either AlAs or InSb interfaces can be forced. SLs grown with InSb-like interfaces generally exhibit superior properties to those with AlAs-like interfaces. Using the more reactive As_2 dimers, it is also possible to grow strain-compensated SLs having mixed interfaces without additional soak times [46]. The interface composition can then be influenced via the group-V flux ratio during the SL growth, and thus the residual group-V concentration of the previous layer. The InAs layers are usually Si-doped, with decreasing concentration towards the active core to reduce internal losses.

The lower cladding layer is followed by the lower GaSb SCL. Since the GaSb layer quality is improved at temperatures higher than 450 °C [47], ramping the substrate temperature to about 480 °C for this growth provides a smoother surface for the subsequent cascaded active region, whose optimal growth conditions are determined from photoluminescence (PL) test samples. The PL emission intensity is generally maximized and the linewidth minimized at active-region growth temperatures in the 430 °C to 480 °C range [48,49,50,51,52], with the most recent studies suggesting temperatures toward the lower end of that range. Another critical parameter is the As flux during the active QW growth, since the presence of a high As background in the growth chamber tends to roughen the InAs/GaInSb interface and decrease the oscillator strength. The negative consequences of As incorporation at the interfaces have also been verified via Fourier-transformed photoluminescence, photoreflectance, and high angle annular dark field scanning tunneling transmission microscopy [53]. An As flux just sufficient to stabilize the As-rich (2x4) reconstruction during the InAs layer growth is recommended.

After the active stages, the upper SCL is grown, with the growth performed at an elevated substrate temperature for the samples grown at the University of Würzburg and at the same temperature for the samples grown at NRL, followed by the upper InAs/AlSb SL cladding for which the temperature is ramped down again for the University of Würzburg samples. For substrate temperatures below 480°C, no degradation in the active stages, e.g. due to intermixing, has been noted. The structure is completed with a highly Si-doped (~ 1 x 10^{19} cm^{-3}) InAs cap layer that forms a low resistive ohmic contact. In addition, graded transition SLs are inserted at the boundaries between the various regions of the full ICL structure, in order to avoid parasitic voltage drops as discussed above.

Figure (a) presents a scanning electron microscopy (SEM) micrograph of a 10-stage ICL. Figure 5(b) shows a typical high-resolution X-ray diffraction (HR-XRD) curve of a 5-stage ICL. The central peak for the SL cladding layers is almost coincident with the substrate peak, indicating well-lattice-matched growth. The small higher-order active region peaks also confirm high growth quality.

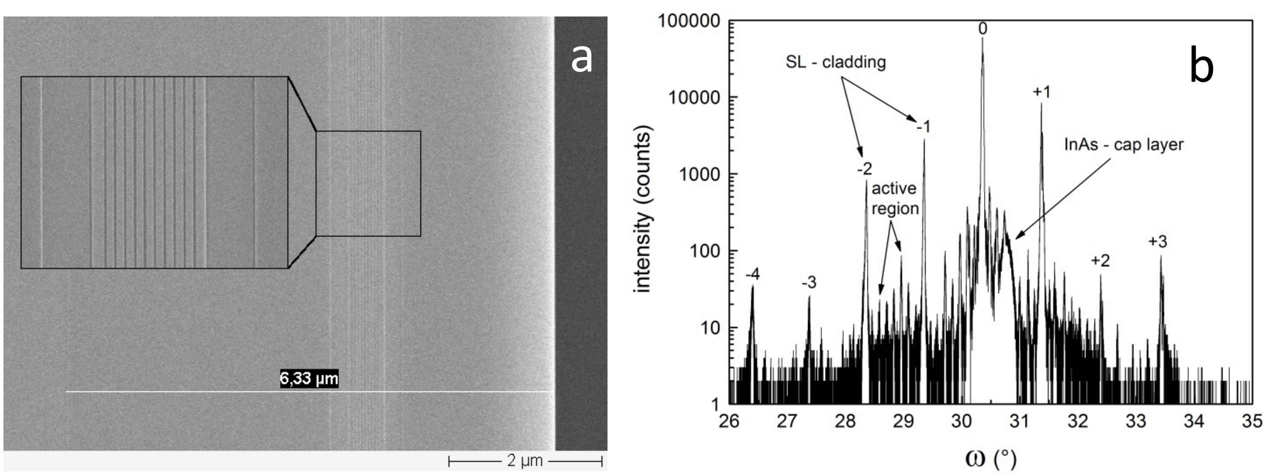

Figure 5: a.) SEM micrograph from the edge of a cleaved ICL wafer. b.) Typical HR-XRD spectrum of a 5 stage ICL ([004] reflection). The sharp high-intensity peaks correspond to the SL cladding, while the smaller, closely-spaced features correspond to the active cascades. The broad peak to the right of the central peaks arises from the 20-nm-thick InAs cap layer.

b. Processing

The ridges for edge-emitting ICLs are generally defined using reactive ion etching based on a Cl- and Ar- plasma. The dry etch is typically followed by a clean-up phosphoric wet etch step that smooths the sidewalls and removes contaminants. Due to highly-anisotropic transport in the superlattice cladding and active regions of an ICL, especially below threshold where the active core has especially high impedance along the vertical axis, the etch must proceed to below the active core to avoid excessive current spreading. Otherwise, the threshold current and efficiency vary strongly with etch depth, ridge width, and stage multiplicity. For example, J_{th} for a 100-μm-wide broad area 5-stage ICL emitting at 3.75 μm was 232 A/cm^2 when the etch proceeded through the active region to the lower SCL, whereas it increased to 286 A/cm^2 when the etch extended only into the 200-nm-thick upper SCL. When the etch was only 1.4 μm deep, into the 2.2-μm-thick upper cladding region, J_{th} increased even further, to 350 A/cm^2 (corresponding to a 50% larger pumped area). For much narrower ridges with 4.5 μm width, a seven-fold increase in the threshold current density was observed when the etch was stopped above the active stages [54].

Broad-area lasers are suitable for measuring such basic characteristics as the emission wavelength of an MBE-grown ICL wafer. These devices are highly reproducible and fast to fabricate. No sidewall passivation is necessary if the etch is shallow, although the threshold current density is then overestimated and the slope efficiency underestimated due to current spreading. It is also possible to process broad-area lasers for pulsed testing using photolithography and wet chemical etching to the bottom SCL layer, without any passivation of the sidewalls, as long as the ridge is wide enough to make a metal contact on top. This process is also relatively quick and convenient, and minimizes the effect of current spreading on the lasing thresholds and slope efficiencies [55].

To mitigate leakage or oxidation at the sidewalls of an ICL that is etched through the active region, passivation is typically employed to suppress excessive short-circuiting currents. State-of-the-art ICLs use a combination of sputtered Si_3N_4 and SiO_2 [56], with an overall thickness of approximately 300-500 nm. Al_2O_3 and MgO may be suitable alternatives with better thermal conductivity, although no comparative studies have yet been carried out. Thermal management is quite critical to the ICL performance, since the thermal conductivities of the active core and short-period InAs/AlSb superlattice cladding regions are low and highly anisotropic. Using the 3ω method, the in-plane and cross-plane thermal conductivities were measured recently [57]. This showed the cross-plane thermal conductivity of the SL cladding layers to be particularly low, in the 1–3 W/mK range. To expedite heat removal from the active region, and thereby increase the maximum operating temperature and output power, ≈ 5 µm of gold is typically electroplated on top of ICL narrow ridges [58]. Lanes of width ≈ 50 µm are left unplated, however, to assure high facet quality following the cleave. Figure 6 shows an SEM micrograph of a 11.8-µm-wide ridge with electroplated gold on top. The dark areas depict the insulating passivation layer which is opened on top of the ridge for contacting. The thermal dissipation can be enhanced further by mounting the ICL ridges epitaxial side down [59].Heat is then directly transferred from the ridge to the heat sink, without passing through the substrate.

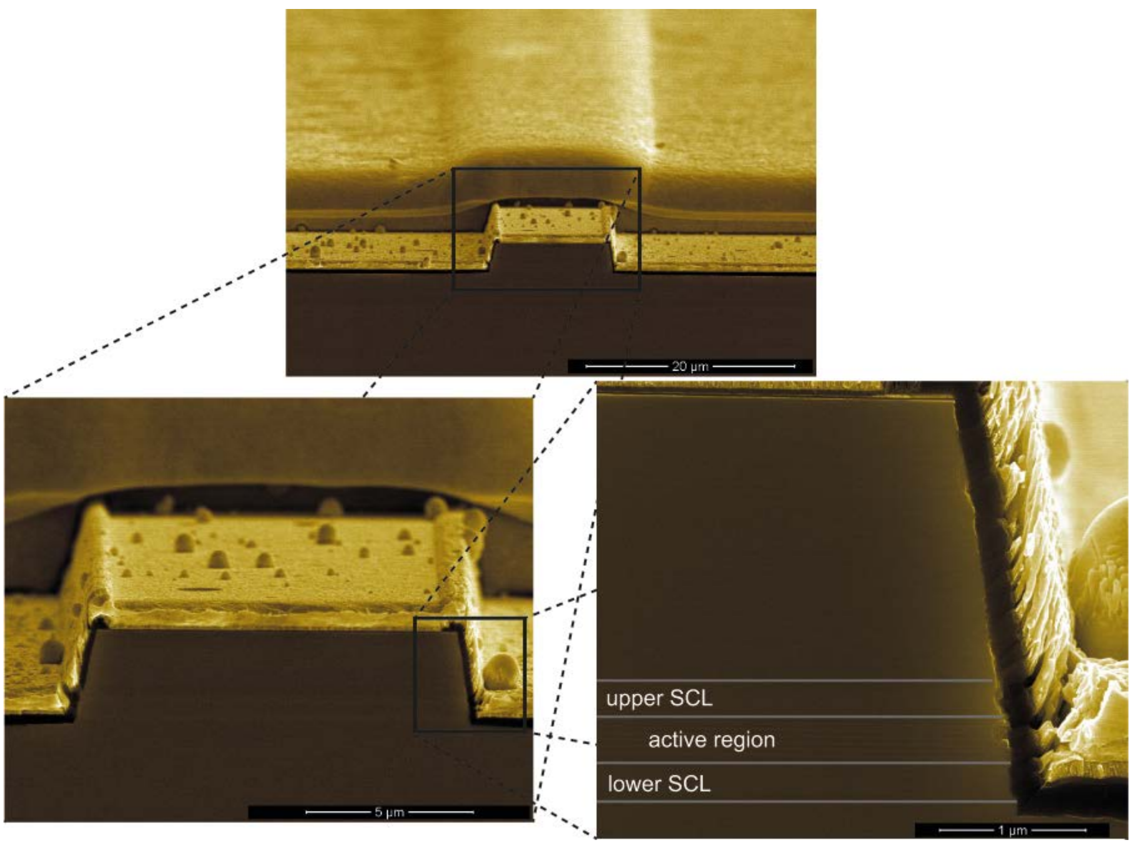

Figure 6: SEM micrograph of a processed 11.8 µm wide ICL rigde with a 5 µm thick electroplated gold layer. The etch proceeded right through the lower SCL. In the highest magnification, the SCL layers and the active region can be identified.

Bauer *et al.* discuss several DFB laser concepts [60] (see also Section 4.d.) that require additional processing steps. In the case of vertical sidewall gratings, the periodic modulation (typically 4th order) can be produced in the same step as the ridge via optical lithography or electron-beam lithography. Other DFB concepts employ 1st-order gratings and require a greater processing effort: In the case of a top grating a 200-nm-thick germanium layer is deposited on top of the ridge and periodically patterned with electron-beam lithography [61]. After a lift-off step, the top contact is evaporated. For the processing of loss-coupled DFBs based on lateral metal gratings [62], a 30 nm Si_3N_4 layer is sputtered on the ridge to prevent short circuiting of the active region. Afterwards the metal grating is defined via electron-beam lithography in Poly(methyl methacrylate) (PMMA) resist, with the subsequent evaporation of chromium and a lift-off step. The final steps, including passivation, contact evaporation, and gold electroplating, are the same as in the processing of narrow ridges.

4. Experimental status

a. Broad area laser performance (pulsed)

The intrinsic performance of a grown ICL structure may be estimated from measurements in pulsed mode at low duty cycle, for which the device heating due to current injection is avoided. Typical pulses are 100–300 ns at a repetition rate in the 1-10 kHz range. Additionally, ridge widths > 100 µm are generally used to minimize the influence of leakage currents and optical losses at the etched sidewalls. Unless stated otherwise, the results presented in this section are based on 2-mm-long and 150-µm-wide devices with untreated facets. Figure 7 shows wavelength-dependent threshold current densities for broad area ICLs with different stage multiplicities operated at 300K. The structures were grown at NRL and UWUERZ, and employed designs with carrier rebalancing in order to minimize J_{th}. Threshold current densities below 500 A/cm^2 were achieved throughout the 2.8 to 5.2 µm wavelength range.

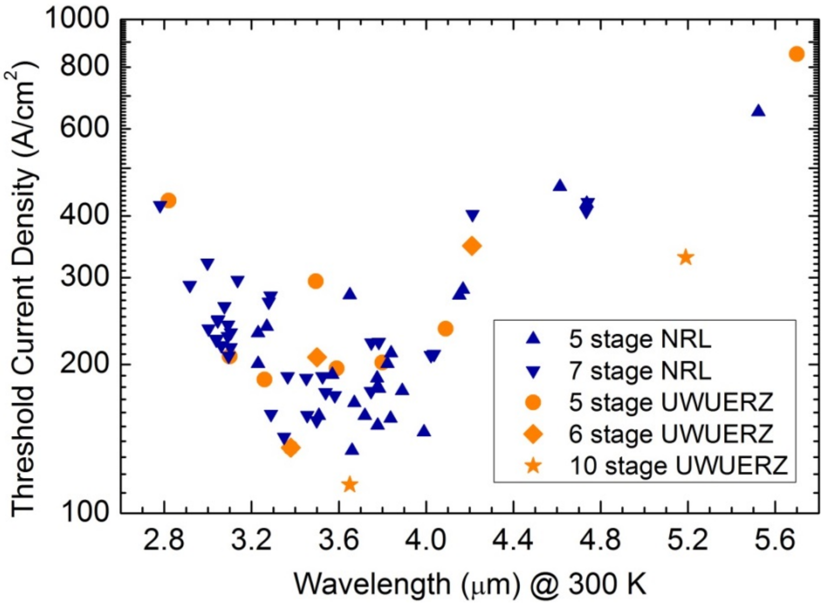

Figure 7: Pulsed threshold current densities for broad area ICLs with various stage numbers at 300 K.

Much of the work to date on optimizing the ICL designs for high performance has concentrated on the 3-4 µm wavelength region, for which a threshold current density as low as 134 A/cm^2 at 300 K was obtained for a 5 stage device emitting at λ = 3.6 µm. At wavelengths shorter than 3.1 µm, J_{th} increases somewhat to above 200 A/cm^2. The threshold also increases at wavelengths longer than 4.1 µm, where J_{th} ~ 400 A/cm^2 at 4.7 µm and 650 A/cm^2 at 5.5 µm [63]. Since only a few ICLs have been grown in the wavelength regime greater than 4 µm, the active core and waveguide designs of those structures may not yet be fully optimized. The temperature increase of J_{th} is represented by the characteristic temperature T_0, which typically ranges from 45 - 60 K in the temperature range from 290 to 350 K. For wavelengths longer than 4 µm, T_0 tends to decrease to 40-45 K. The lowest threshold current density for an ICL (114 A/cm^2 @ 300K) was reached with a 10 stage device emitting at 3.65 µm [64]. Furthermore, a 10-stage ICL emitting at 5.2 µm exhibited considerably lower J_{th} than any of the devices with fewer stages and emitting at wavelengths as much as 1 µm shorter. The general increase of the external quantum efficiency with increasing stage multiplicity [53] also makes such devices interesting for high-power applications.

To further investigate the influence of the number of stages (M) on the lasing characteristics, a series of ICLs with stage multiplicities varying from 1 to 12 was grown within a period of less than two weeks. The fixed active region was similar to the one used in [27], since that design had already performed well in 5-stage devices. For the purpose of carrier rebalancing, the inner 4 of the 6 InAs electron injector wells were heavily doped with Si to a density of 5 x 10^{18} cm^{-3}. The "W" active quantum wells were designed to emit at a wavelength of 3.6 µm. The inset of Fig. 10 (below) shows the emission spectrum from a 4-stage broad area ICL when operated at room temperature in pulsed mode (1 kHz repetition rate, 200 ns pulse width). All of the devices in this series with varying *M* emitted at wavelengths between 3.54 µm and 3.68 µm. This indicates a highly stable In effusion cell flux, since the emission wavelength is extremely sensitive to the InAs layer thicknesses in the active QWs [65].

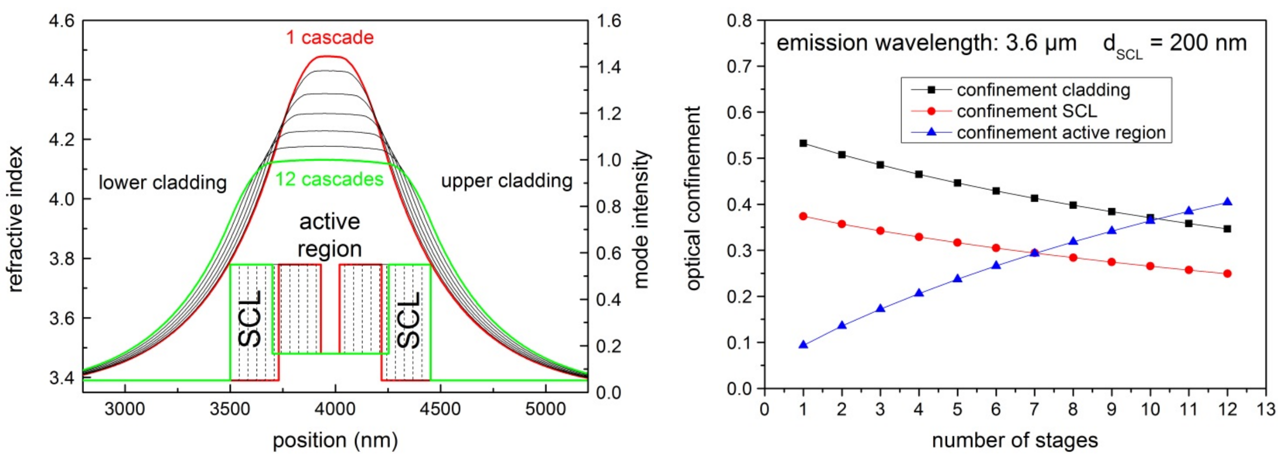

Figure 8: Optical mode profiles (left) and confinement factors in the claddings, SCL and active regions (right), for ICL waveguides with stage numbers from 1 to 12.

The active stages were embedded in 200-nm-thick GaSb separate confinement layers doped with Te to a level of 3 x 10^{17} cm^{-3} on both sides. The lower and upper cladding thicknesses were 3.5 µm and 2.0 µm, respectively. Since the active region thickness varied with the number of stages, the optical mode profiles change. The left panel of Figure 8 shows calculated optical mode profiles for *M* = 1, 2, 4, 6, 8, 10 and 12. In this figure the mode and refractive index profiles are shifted to the right in order to center all modes at the same position, even though the lower cladding has the same thickness for all stage numbers. For higher stage multiplicities a greater fraction of the optical mode overlaps the active core, whereas the modal overlap with the SCL and SL-cladding layers decreases. Figure 8 (right) plots the modal confinement of the different regions as a function of stage number. The overlap with the active region increases from 0.095 for one stage to 0.404 for 12 stages, while the overlap with the SCLs and cladding are reduced from 0.374 to 0.249 and from 0.532 to 0.347, respectively. It should be noted that the active region confinement in [64] was underestimated since the refractive index of GaSb was taken to be 3.73, whereas ellipsometry measurements have shown 3.78 to be more accurate. The increased modal confinement in the active region for larger stage numbers implies that a higher modal gain and thus lower threshold current density should be expected. Notice also the different (single-humped) mode profiles obtained when 200-nm-thick SCLs are employed here as opposed to the 800-nm-thick SCLs employed in generating Figure 3, as well as the much lower confinement in the SCLs and higher confinement in the active and clad regions as compared to the thicker SCLs in Fig. 4.

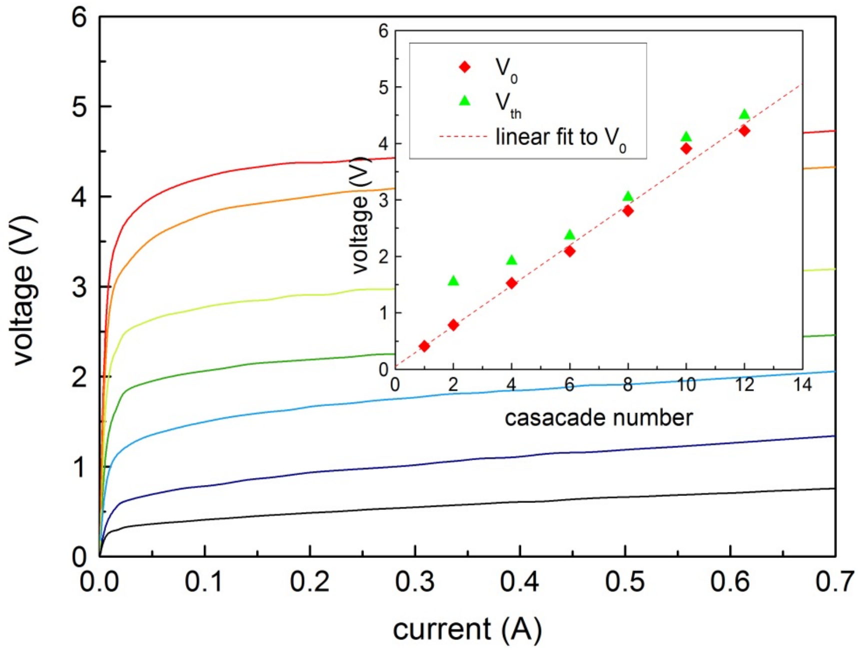

Figure 9: *I*-*V* characteristics of 150-μm-wide and 2-mm-long broad area devices with different stage multiplicities at $T = 20^{o}$C. The inset shows the corresponding values for the intercept of the linear part of the *I*-*V* curve (V_0) and threshold voltage V_{th}.

The threshold voltage should scale almost linearly with M, since additional stages require that more bias (at least $\hbar\omega$ per stage) be applied to tilt the band structure. Figure 9 shows the measured *I*-*V* characteristics for broad-area lasers with different stage numbers at room temperature. At low currents, the resistance remains very high until the electric field becomes large enough to properly align the energy levels within the active stages. However, once the highly conductive regime is reached, the series resistance decreases to < 1 Ω. The inset of Figure 9 plots the dependence on M of the voltage at which current starts to flow through the structure (V_0) and the threshold voltage (V_{th}). The broken line indicates that V_0 increases almostlinearly with M. That the curve intercepts the ordinate just above zero, at 0.16 V, indicates that most of the bias drops across the cascaded stages while only a low residual fraction can be attributed to the contacts and transition regions between the SCLs and claddings. For M > 6, V_{th} behaves similarly to V_0, but is slightly higher due to the series resistance and contributions of order $M \times k_B T$ that are needed to overcome losses. In the case of lower stage multiplicities, V_{th} deviates more strongly from the linear trend because the threshold current density is higher. In the limit $M = 1$, V_{th} could not be investigated since laser operation was not observed at $T = 20^oC$.

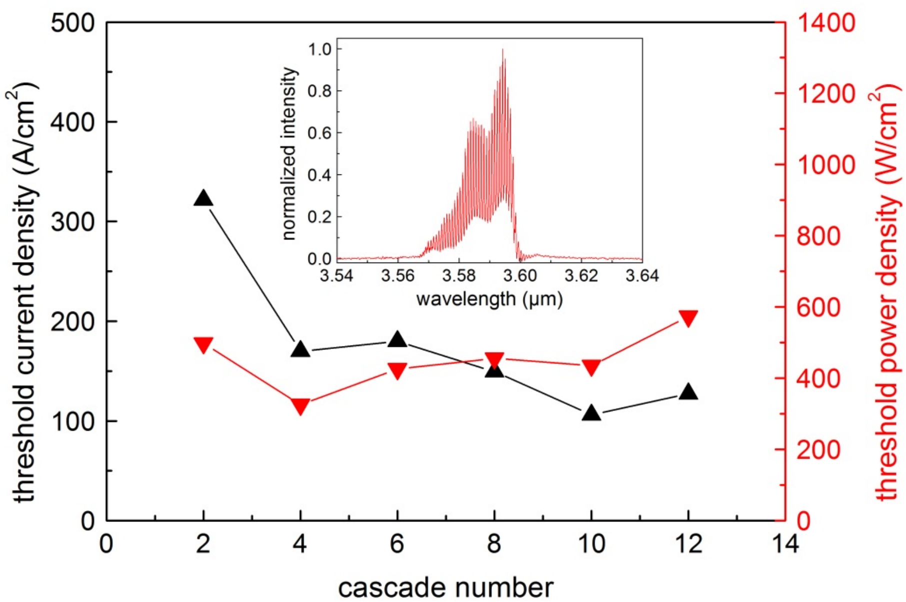

Figure 10: Threshold current density and threshold power density for a series of broad area ICLs (2 mm x 150 µm) at $T = 20^oC$ with stage multiplicities M ranging from 2 to 12. The inset shows the emission spectrum for a 4-stage broad area laser operated at room temperature in pulsed mode.

To enhance the statistics for the threshold values, at least five 2-mm-long lasers with each M were characterized. Figure 10 plots the resulting average values of J_{th} and P_{th} at $T = 20^oC$. A general trend towards lower threshold current densities for higher stage numbers is observed. The highest value of 322 A/cm^2 was measured for the 2 stage laser, whereas J_{th} for the 4 stage device already drops to 170 A/cm^2, which can be attributed to the strong increase of modal gain and reduced loss. With further increase of the stage number, J_{th} continues to decrease modestly due to the higher modal gain. The lowest average value of 106 A/cm^2 was achieved for the 10 stage ICL, and several lasers with M = 10 exhibited J_{th} slightly below 100 A/cm^2. The threshold for the 12 stage laser increased slightly, to 127 A/cm^2. However, the reduction of J_{th} at high M comes at the price of a monotonically increasing V_{th} (Figure 8). This leads to a very different picture for the M dependence of the threshold power density, an important figure of merit in applications requiring low power consumption. The lowest P_{th} of 326 W/cm^2 was measured for the 4 stage device.

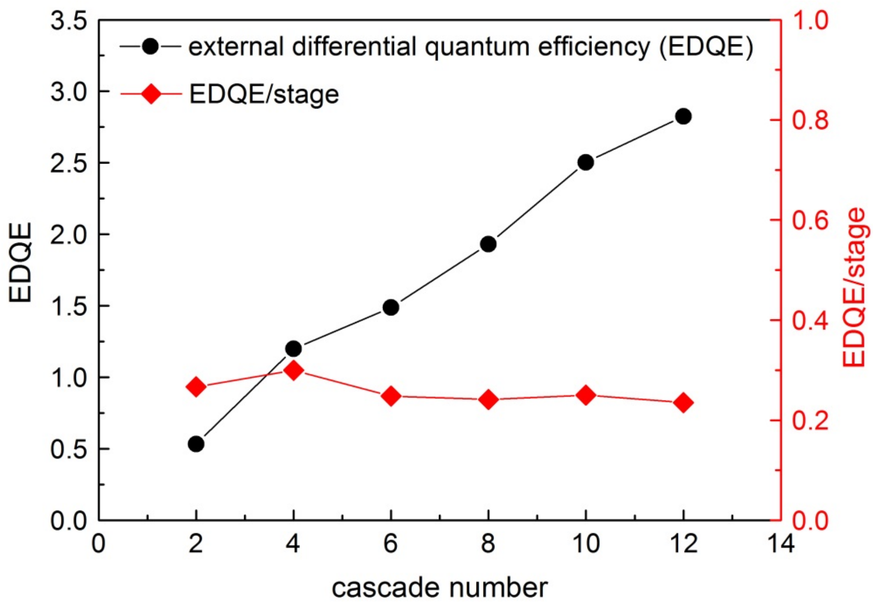

Figure 11: Net external differential quantum efficiencies (black points, left scale) and EDQE per stage (red points, right scale) at T = 20°C for the series of broad area ICLs (2 mm x 150 µm) with stage numbers ranging from 2 to 12.

Figure 11 plots the total EDQE (from all stages) *vs*. M for the series of broad area lasers when operated in pulsed mode at T = 20°C. The EDQE scales with M, as expected. Also plotted is the EDQE per stage, which stays nearly constant in the range 24-30%, and decreases only gradually at higher stage numbers. This indicates that the overall loss is nearly independent of M, which in turn implies that the losses contributed by the three main parts of the waveguide (active region, SCL, and cladding) are weighted roughly equally. It was shown in [55] that the slope efficiency can exceed the stage number proportionality when the overall loss is reduced, in particular by using thick and very-low-doped SCLs, along with careful design optimization of the optical mode overlap with the different waveguide parts.

This led to improvement of the slope efficiency (from 2 facets) for broad area devices from 620 – 680 mW/A for 5 stage devices to values near 1200 mW/A for 7-stage ICLs. That the increase is larger than 7/5 indicates that the net loss was reduced, due to the shift of a portion of the optical mode out of the cladding layers and into the low-doped SCLs.

The results of the cascade variation study clearly show that there is still room for optimization. However, the optimal stage multiplicity also depends on which figure of merit is given the greatest weight. While mobile applications will benefit from the low threshold powers of devices with low M (Figure 10), high-power applications will benefit from the higher net EDQE associated with a larger M (Figure 11).

b. Ridge waveguide laser performance (cw)

To ensure sufficient heat dissipation, and to avoid the occurrence of higher-order lateral modes, narrow ridges have been fabricated for operation in cw mode. After chip fabrication the lasers are mounted on c-mounts, either epitaxial side up or down. In the first case, heat dissipation is mainly achieved by lateral heat flow in the electroplated gold layer on top of the structure, whereas in the latter case heat is more efficiently transferred directly to the copper mount. The advantage of epi-down mounting can be quantified by the thermal impedance-area product (R_tA), which can be extracted from the P-I-V characteristics. While the values measured for epi-up-mounted devices (ridge width varying from 7.7 to 15.7 µm) were in the range 5.1 to 8.6 K/(kW/cm^2), the R_tA for epi-down-mounted devices with the same dimensions decreased to 3.3-5.2 K/(kW/cm^2) due to better heat removal. To enhance the output power and wallplug efficiency, the facets are commonly coated with high reflection (HR) and anti-reflection (AR) layers having reflectivities of > 95 % and ≈ 1-2%, respectively. The first carrier rebalanced and epi-up-mounted 5-stage narrow ridge devices lased in cw mode up to a maximum operation temperature (T_{max}) of 107 °C [27], with typical output powers of ≈ 50 mW at room temperature. The threshold power for a 0.5-mm-long laser was only 29 mW [27], by far the lowest for a semiconductor laser emitting in the 3-4 µm range.

Epi-down mounting substantially improves the maximum output power (P_{max}^{cw}) and wallplug efficiency (WPE) [66]. The left side of Figure 12 shows the *P-I-V* characteristic of an epi-down-mounted 15.7-µm-wide and 4-mm-long device operating at 25 °C. The low J_{th} of 156 A/cm^2 and V_{th} of 2.3 V are comparable to the values measured for broad-area devices processed from the same wafer, indicating that the degradation due to processing and mounting was minimal. At an injection current of 1.2 A, the maximum output power was 253 mW. The beam quality determined from the far-field profiles illustrated on the right side of Fig. 12 is represented by M^2 = 2.2 at I = 0.4 A and M^2 = 2.7 at I = 1.2 A.

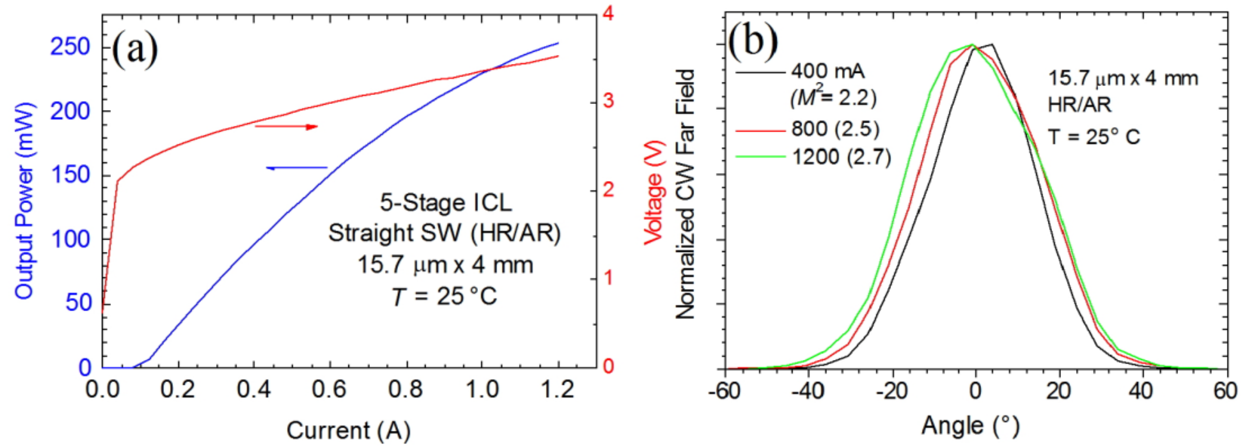

Figure 12: *P-I-V* characteristics of an epi-down-mounted 15.7-µm-wide, 4-mm-long ICL with HR and AR facet coatings operating in cw mode at 25°C (left). Far-field patterns of same device at different injection currents (right) [64].

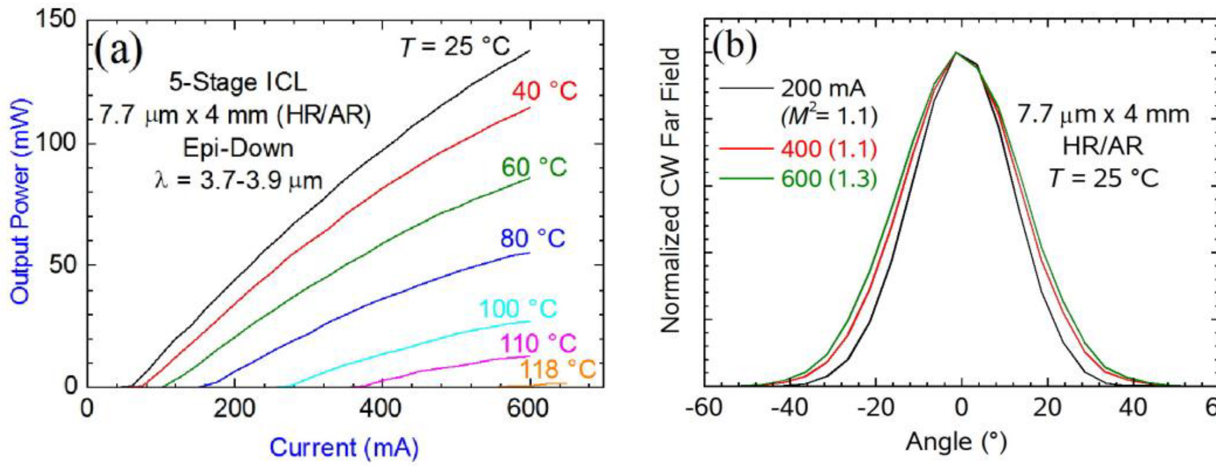

Figure 13: *P-I-V* characteristics of an epi-down-mounted 7.7-µm-wide, 4-mm-long ICL with HR and AR facet coatings operating in cw mode at various operation temperatures [64] (left). Far-field patterns at different injection currents for a 15.7-µm-wide and 4-mm-long device with HR and AR facet coatings mounted epi-side-down (right).

Narrowing the ridge width generally improves the beam quality, but at the expense of higher J_{th} and lower output power. For example, a 7.7-µm-wide ridge showed a slightly elevated J_{th} of 184 A/cm^2 due to sidewall carrier recombination, but operated in cw mode up to T_{max}^{cw} = 118 °C [64]. The *P-I* characteristics at different operating temperatures are shown in Figure 13 (left). The device emitted a nearly ideal Gaussian beam at all injection currents, *e.g.*, M^2 = 1.1 at 200 mA and M^2 = 1.3 at 600 mA. The WPE tends to be maximized in short cavities for which the internal loss is comparable to the mirror loss. Figure 14 shows the *P-I* curves of two short cavities, along with their WPEs *vs*. current. A WPE of nearly 15% is reached for the 0.5-mm-long cavity at 76 mA, which compares to the highest value of 21% reported for QCLs (λ = 4.8 – 4.9 µm) at room temperature [67]. Very recently, NRL ICLs with 1-mm-long cavities and both 7 and 10 stages attained 18% WPE [68].

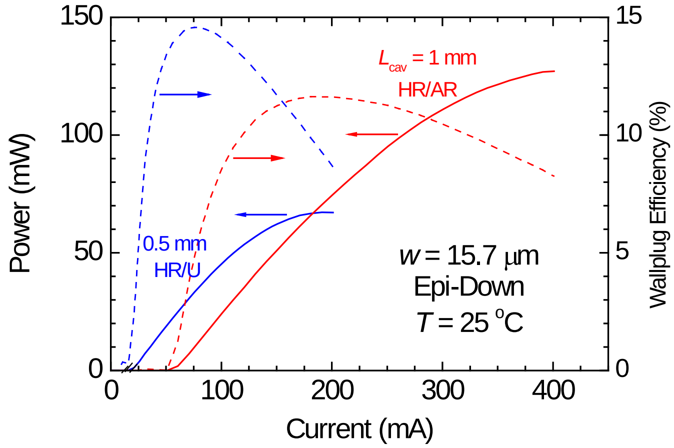

Figure 14: Output power and WPE *vs*. current for two 15.7-µm-wide devices. The 0.5 mm long cavity had one HR and one uncoated facet, while the 1 mm long cavity had an HR-coated back facet and AR-coated front facet [64].

The cw operation of ICLs at RT is not limited to the 3-4 µm wavelength range. A maximum operation temperature of 60 °C was obtained for a 4-mm-long and 10.9-µm-wide ridge emitting at 4.8 µm. At room temperature, more than 15 mW of cw output power was measured. Another device, with the same dimensions and processed from a different wafer, lased in cw mode up to 48 °C at λ = 5.6 µm with similar output powers [61].

c. Power Scaling

An important class of potential applications requires high output powers. The maximum output power for ICLs generally scales with the ridge width, since the threshold power density and thermal impedance tend to decrease for wider ridges. However, this can break down when the lower lateral thermal dissipation leads to excessive heating caused by a high threshold power. A more fundamental drawback of power scaling via ridge width is the degradation of beam quality that results from lasing in higher-order lateral modes. To combine high ICL output power with nearly diffraction limited beam quality, two distinct concepts have been investigated to date. The results may be quantified in terms of the "brightness" figure of merit (B) defined as P_{out}/M^2.

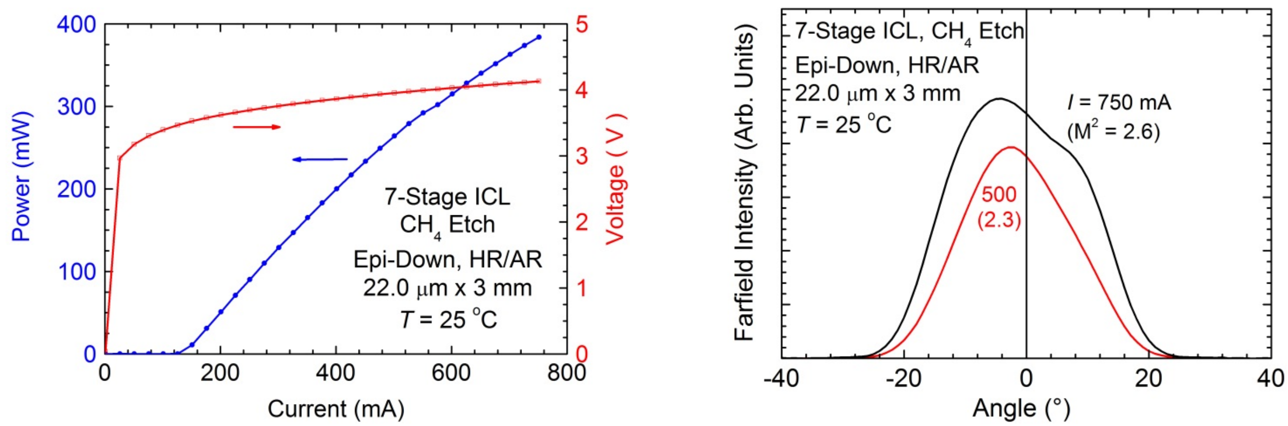

Figure 1: Left: Light-current characteristics in cw mode for a 22.0-µm-wide, 3-mm-long 7-stage ICL mounted epi-side-down with an HR coating on the back facet and an AR coating on the front facet at a temperature of 25°C. Right: Far-field profiles of the same ridge at different current injection levels.

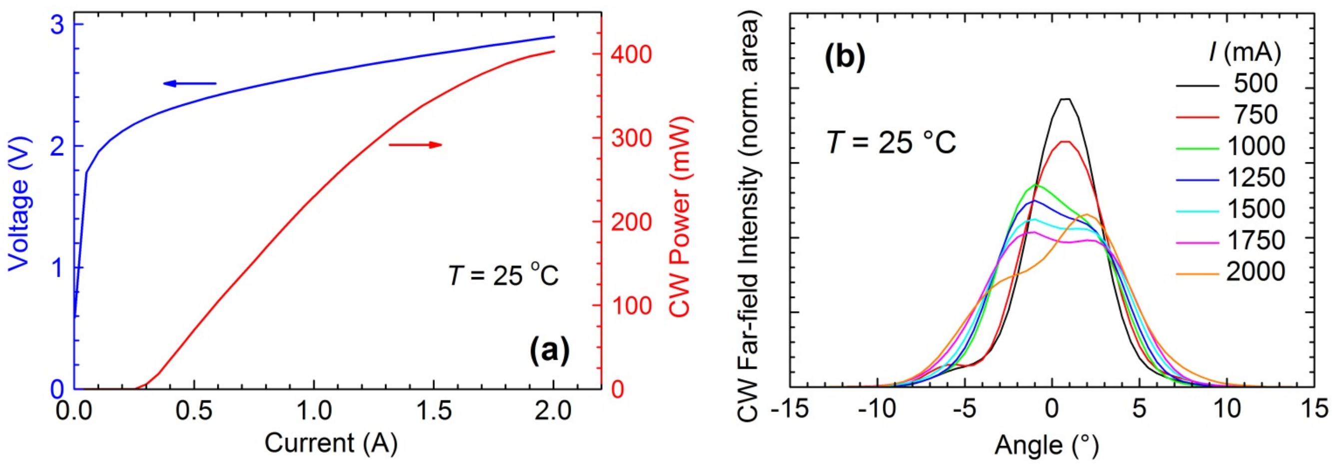

Figure 16: Left: Cw *P-I* characteristics for a tapered-ridge ICL at $T =$ 25°C. (b) Cw far-field emission profiles at a series of injection currents. The extracted M^2 values range from 1.4 at I = 0.5 A to 2.3 at I = 2 A [69].

The first concept introduced corrugations into the etched ridge sidewalls. Since higher-order modes have greater overlap with the sidewalls, they experience increased scattering losses and are hence selectively suppressed relative to the fundamental mode. At the same time, it is advantageous to minimize the overlap of the fundamental mode with the corrugations, in order to reduce the impact on the laser efficiency. Ridge waveguide lasers with 5 and 7 stages were processed with corrugated sidewalls (typical peak-to-valley amplitudes of 1.4 µm and periods of 2.0 µm). Generally the 7-stage devices showed higher output power, due in part to their higher differential output power but also because of a lower internal loss (see the discussion near the end of Section 4.a). The left side of Figure 15 shows the room temperature *P-I* characteristics of a 22.0-µm-wide and 3-mm-long 7-stage device with HR/AR coated facets. The output power reached 384 mW with high beam quality (M^2 = 2.6), and with a WPE of 12.4 % at P_{max}^{cw}. While minor deviations of the far-field peak from zero may be due to alignment imperfections, the larger asymmetries shown in Fig. 15 may reflect phase locking of the lateral modes [69].

Number of stages	Ridge width (µm)	Sidewalls	Output power (mW)	Effective M^2	Brightness = Power/M^2
5	7.7	straight	138	1.3	106
5	10.8	straight	198	1.8	110
5	15.7	straight	254	2.7	94
5	13.2	corrugated	102	1.2	85
5	18.2	corrugated	205	1.6	128
5	25.1	corrugated	274	2.2	125
5	25.2	corrugated	291	2.2	132
5	tapered (5.5/63)	corrugated	403	2.3	175
5	tapered (5/57)	corrugated	264	1.8	155
7	22	corrugated	383	2.4	160
7	32	corrugated	592	3.7	160

Table 1: Maximum cw-output powers, M^2 values, and brightnesses for various high-power ICLs, including structures with variable ridge width, corrugated sidewalls, and tapered ridges with 5 and 7 stages.

A second option for increasing the output power while maintaining high beam quality is to taper the ridges [70,71]. When this concept is applied to near-IR lasers, a narrow waveguide that supports only one lateral mode is combined with a gain-guided tapered section (typical half angle ≈ 3°) that increases the pumped area. As described above, the ICL's extensive lateral current spreading makes it mandatory to etch through the active core, although index-guided structures have been fabricated from 5-stage IC material. Figure 16 (left) shows the *P-I* characteristics of a tapered ICL [72]. The device was 4 mm long, with a back facet aperture of 5.5 µm, front facet aperture of 63 µm, and taper half angle or 0.42° (resulting in a net pumped area of 0.00139 cm^2). Sidewall corrugations were applied to the wider part of the ridge to further suppress lasing in higher-order later modes. The device had J_{th} = 210 A/cm^2 and emitted up to 403 mW of cw output power at I = 2 A. The right panel of Figure 16 show the normalized far-field profiles of that device. The measured beam quality factors ranged from $M^2 = 1.4$ at $I = 0.5$ A to $M^2 = 2.3$ at $I = 2.0$ A. The resulting brightness of $B \approx 175$ mW was 28% higher than the best previous ICL result (for a 5-stage ICL with 25 μm wide ridge and corrugated sidewalls [66]). Collected results for the output power, beam quality and brightness of various high-power ICLs are presented in Table 1.

d. Single Mode Devices

In addition to compactness, robustness and low power consumption, spectroscopic applications demand a spectrally narrow line width, and thus emission in a single longitudinal mode [58]. Several concepts have been studied to allow ICLs to emit in a single mode for cw operation at room temperature. In 2008, a photonic-crystal distributed feedback (DFB) ICL emitted 67 mW of cw output power in a single mode (λ = 3.27 μm) at a temperature of 78 K [73]. To confine current and the optical mode, the region outside the gain section was bombarded with helium ions. One year later, the first cw DFB ICL emission at room temperature was achieved by employing a corrugated sidewall grating that on the one hand served to suppress higher-order lateral modes and on the other provided distributed feedback for selection of a single longitudinal mode. With a 4th-order grating etched into the ridges sidewalls [74], cw emission in a single mode was achieved up to T = 40°C. More recently, a corrugated-sidewall DFB ridge with 13.2 μm width and 4 mm length emitted up to 55 mW in a single spectral mode at 25 °C [26]. In 2014, a DFB ICL of this kind was realized in the 5.2 μm wavelength region for sensing nitric oxide sensing with a room-temperature drive power of only 138 mW [75]. An advantage of the vertical sidewall grating approach is that it can employ optical rather than electron-beam lithography. However, it is not very robust since the coupling strength is quite sensitive to ridge width and the fill factor of the grating. The use of a third-order rather than four-order grating would solve the latter issue, but would be more challenging to fabricate with optical lithography.

The option of etching the DFB grating into a Ge layer deposited on top of the ridge provides a coupling coefficient that does not depend significantly on the ridge width. That approach was applied to ICL gain material in 2007 [76], and more recently produced robust cw emission in a single mode at $\lambda \approx$ 3.8 μm for temperatures up to 80 °C [77]. Figure 17 shows an SEM micrograph of a ridge with a 1st-order

Ge grating on top. Figure 18 illustrates the single-mode emission spectra at a series of temperatures and a fixed drive current of 170 mA (left), together with *P-I-V* characteristics for the 2-mm-long and 7.4-µm-wide device (right). Up to 27 mW of single mode output power was realized at $T = 40°C$. Typical temperature and power tuning rates were 0.39 - 0.40 nm/°C and 12 nm/W, respectively, with a total tuning range of > 25 nm. Even though the top grating approach is very robust, its primary disadvantage is a higher optical loss resulting from the modal overlap with the top contact metallization. Since the grating coupling coefficient is also proportional to this overlap, it is inevitable that the threshold power density will increase and the slope efficiency decrease.

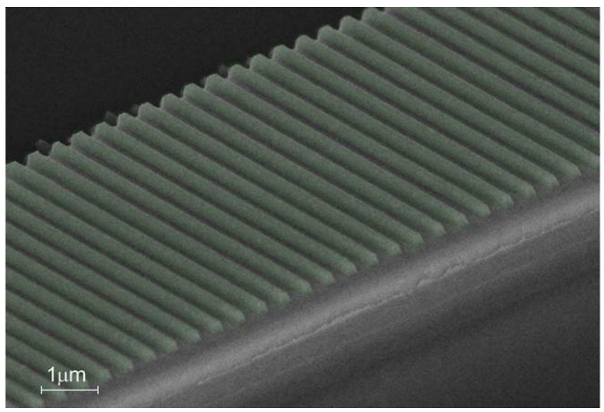

Figure 17: False-color SEM micrograph of a 7.4 µm wide ridge with a first order Ge top grating.

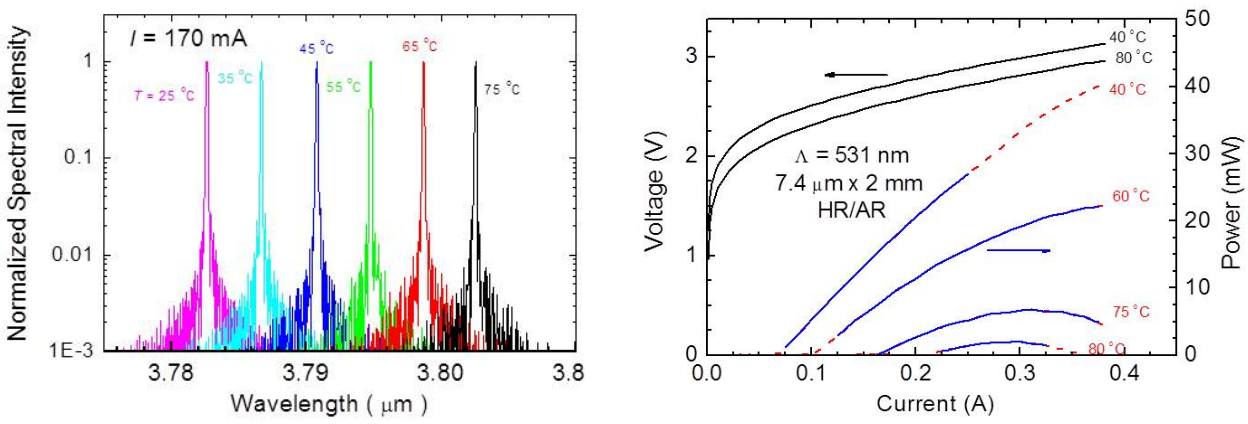

Figure 18: Left: Emission spectra of a 7.4-µm-wide and 2-mm-long HR/AR-coated ICL ridge topped by a Ge DFB grating, at a drive current of 170 mA and a series of temperatures. The first-order grating period was 531 nm. Right: *P-I-V* characteristics of the device at several temperatures. The solid and dashed portions of the power curves correspond to single- and multi-mode emission, respectively [74].

In 2014, two additional concepts for achieving single mode emission from an ICL were demonstrated. In the first, a laterally coupled DFB was fabricated by etching the ridge in two steps [52]. These devices produced up to 18 mW of cw single-mode output at λ = 3.57 μm and a temperature of 46 °C. Lifetime measurements at T = 40 °C found negligible degradation of the output when four devices were operated for more than 8800 hours. A second, loss-coupled, approach employed metal gratings deposited next to the ridge [78]. That approach also provided single-mode cw emission at temperatures above ambient.

5. Future prospects

ICLs have proven to be a practical mid-IR source for a variety of applications, and are especially attractive when very low power consumption is required. Most of the work to date has concentrated on the wavelength region between 3 and 4 μm, where the threshold current and power densities appear to be approaching the theoretical limits. Moreover, it may be difficult to substantially further reduce the optical losses that have already come down to a few cm^{-1}. Nevertheless, additional optimization of the active region design may lead to somewhat better performance.

On the other hand, there is clearly room for improving the performance in spectral regions outside the ICL's established central "sweet spot", *i.e.*, at λ < 3 μm and > 4 μm where little optimization has been attempted to date. Both the cascade designs and configuration of the waveguides for higher gain and/or lower loss need to be investigated. Further work will also help to optimize the number of cascades *vs*. wavelength for applications requiring either low power consumption or high output power as the primary figure of merit. While to minimize the drive power it is presumably beneficial to employ a smaller number of active stages, even in those applications the optimal M may increase somewhat with increasing wavelength (since more gain may be required as the losses increase).

An additional concept, which was introduced as early as 1996 [9] and expanded upon theoretically more recently [79], is to use type-I active transitions in an ICL that benefits from spatially direct radiative emission. Following a very early experimental demonstration in 1998 [80], much better performance was obtained in 2013 when a cw output power of 590 mW was generated by a 100-μm-wide ridge at room temperature for an emission wavelength of almost 3 μm [81]. While this paves the way to the realization of devices emitting to at least 3.4 μm, it remains to be seen how future type-I ICLs will compare with the state-of-the-art type-II devices operating in the same spectral region.

Although the interband nature of the ICL's lasing transition results in the strong absorption on the short-wavelength side of the gain peak that is not present in a QCL [82,83], the ICLs have nonetheless demonstrated wavelength tunability over hundreds of nanometers [84] as well as low-temperature emission at two wavelengths separated by ≈1 μm [85]. This makes them promising for widely-tunable mid-infrared single-mode devices such as longitudinally-coupled DFBs [86,87], lateral DFB arrays [88], coupled cavities [89,90] and sampled gratings [91]. The interband cascade technology should also be adaptable to miniature lab-on-a-chip platforms, on which ICLs and interband cascade detectors [92] are integrated in a monolithic device, as has already been pursued using quantum cascade structures [93].

Finally, in contrast to QCLs, the active transitions couple to transverse-electric (TE)-polarized photons. This makes the ICL compatible with vertical emission without requiring the assistance of a grating. Whereas to date no electrically-pumped vertical-cavity surface-emitting laser (VCSEL) has emitted at a wavelength beyond 2.6 μm [94], interband cascade gain materials could extend that capability throughout the mid-IR spectral band. Interband cascade light-emitting devices (ICLEDs) with 15 stages, but no optical cavity to provide feedback, recently produced > 1 mW cw of non-coherent vertical emission for room-temperature operation at a wavelength beyond 3 μm for the first time [95].

Due to its very low drive power requirement, the ICL is increasingly viewed as the laser of choice for mid-IR (meaning the entire λ = 3-6 μm spectral band) laser spectroscopy applications that do not require high output power but need to be hand-portable and/or battery operated. With ICLs already beginning to find use in fielded systems to detect methane, formaldehyde, and other trace chemicals, it is anticipated that this role will expand substantially over the coming decade.

NRL acknowledges support from the Office of Naval Research. UWUERZ is grateful to the European Union for financial support of this work within the FP7 project “WideLase” (No. 318798). We also thank S. Kuhn, M. Wagenbrenner, S. Handel, and T. Steinl for technical assistance.

6. References

[1] von Edlinger M, Scheuermann J, Nähle L, Zimmermann C, Hildebrandt L, Fischer M, Koeth J, Weih R, Höfling S, Kamp M 2014 DFB interband cascade lasers for tunable laser absorption spectroscopy from 3 to 6 μm *Proc. SPIE* **8993** 899318

[2] Beck M, Hofstetter D, Aellen T, Faist J, Oesterle , Ilegems, Gini E, and Melchior H 2002 Continuous wave operation of a midinfrared semiconductor laser at room temperature *Science* **295** 301–305

[3] Hosoda T, Kipshidze G, Shterengas L, and Belenky G 2010 Diode lasers emitting near 3.44 μm in continuous-wave regime at 300 K *Electron. Lett.* **46** 1455-1456

[4] Belenky G, Shterengas L, Kipshidze G, and Hosoda T 2011 Type-I diode lasers for spectral region above 3 μm *IEEE J. Sel. Top. Quantum Electron.* **17** 1426-1434

[5] Faist J, Capasso F, Sivco DL, Sirtori C, Hutchinson AL, and Cho AY 1994 Quantum Cascade Laser *Science* **264** 553-556

[6] Faist J 2013 *Quantum Cascade Lasers* Oxford University Press, Oxford UK

[7] Bai Y, Bandyopadhyay N, Tsao S, Slivken S, and Razeghi M 2011 Room-temperature quantum cascade lasers with 27% wall plug efficiency *Appl. Phys. Lett.* **98** 181102

[8] Yang RQ 1995 Infrared laser based on intersubband transitions in quantum wells *Superlatt. Microstruct.* **17** 77-83

[9] Meyer JR, Vurgaftman I, Yang RQ, and Ram-Mohan LR 1996 Type-II and type-I interband cascade lasers. *Electron. Lett.* **32** 45-46

[10] Vurgaftman I, Meyer JR, and Ram-Mohan LR 1997 Mid-IR Vertical-Cavity Surface-Emitting Lasers *IEEE J. Quantum Electron.* **34** 147-156

[11] Lin CH, Yang RQ, Zhang D, Murry SJ, Pei SS, Allerman AA, and Kurtz SR 1997 Type-II interband quantum cascade laser at 3.8 μm *Electron. Lett.* **33** 598-599

[12] Yang BH, Zhang D, Yang RQ, Lin CH, Murry SJ, and Pei SS 1998 Mid-infrared interband cascade lasers with quantum efficiencies >200% *Appl. Phys. Lett.* **72** 2220-2222

[13] Felix CL, Bewley WW, Aifer EH, Vurgaftman I, Meyer JR, Lin CH, Zhang D, Murry SJ, Yang RQ, Pei SS 1998 Low-threshold 3.0 mm interband cascade “W” laser *J. Electron. Mater.* **27**77-80

[14] Olafsen LJ, Aifer EH, Vurgaftman I, Bewley WW, Felix CL, Meyer JR, Zhang D, Lin CH, and Pei SS 1998 Near-room-temperature mid-infrared interband cascade laser *Appl. Phys. Lett.* **72** 2370-2372

[15] Bruno JD, Bradshaw JL, Yang RQ, Pham JT, and Wortman DE 2000 Low-threshold interband cascade lasers with power efficiency exceeding 9% *Appl. Phys. Lett.* **76** 3167-3169

[16] Yang RQ, Bradshaw JL, Bruno JD, Pham JT, and Wortman DE 2001 Power, efficiency, and thermal characteristics of type-II interband cascade lasers *IEEE J. Quantum Electron.* **37** 282-289

[17] Yang RQ, Bruno JD, Bradshaw JL, Pham JT, and Wortman DE 2002 Mid-infrared type-II interband cascade lasers *IEEE J. Quantum Electron.* **38** 559-568

[18] Hill CJ, Yang BH, and Yang RQ 2004 Low-threshold interband cascade lasers operating above room temperature *Physica E* **20** 486-490

[19] Yang RQ, Hill CJ, and Yang BH 2005 High-temperature and low-threshold midinfrared interband cascade lasers *Appl. Phys. Lett.* **87** 151109

[20] Mansour K, Qiu Y, Hill CJ, Soibel A, and Yang RQ 2006 Mid-infrared interband cascade lasers at thermoelectric cooler temperatures *Electron. Lett.* **42** 1034-1036

[21] Webster CR, Mahaffy PR, Atreya SK, Flesch GJ, Farley KA, and MSL Science Team 2013 Low upper limit to methane abundance on Mars *Science* **342** 355-357

[22] Canedy CL, Bewley WW, Lindle JR, Kim CS, Kim M, Vurgaftman I, and Meyer JR 2006 High-power and high-efficiency midwave-infrared interband cascade lasers *Appl. Phys. Lett.* **88** 161103-161105

[23] Bewley WW, Nolde JA, Larrabee DC, Canedy CL, Kim CS, Kim M, Vurgaftman I, Meyer JR 2006 Interband cascade laser operating cw to 257 K at λ = 3.7 μm *Appl. Phys. Lett.* **89** 161106

[24] Bewley WW, Canedy CL, Kim M, Kim CS, Nolde JA, Lindle JR, Vurgaftman I, and Meyer JR 2007 Interband cascade laser operating to 269 K at λ = 4.05 μm *Electron. Lett.* **43** 283-285

[25] Kim M, Canedy CL, Bewley WW, Kim CS, Lindle JR, Abell J, Vurgaftman I, and Meyer JR 2008 Interband cascade laser emitting at λ = 3.75 μm in continuous wave above room temperature *Appl. Phys. Lett.* **92** 191110

[26] Vurgaftman I, Bewley WW, Canedy CL, Kim CS, Kim M, Lindle JR, Merritt CD, Abell J, and Meyer JR 2011 Mid-IR type-II interband cascade lasers *IEEE J. Select. Top. Quantum Electron.* **17** 1435-1444

[27] Vurgaftman I, Bewley WW, Canedy CL, Kim CS, Kim M, Merritt CD, Abell J, Lindle JR, and Meyer JR 2011 Rebalancing of internally generated carriers for mid-infrared interband cascade lasers with very low power consumption *Nature Commun.* **2** 585

[28] Vurgaftman I, Bewley WW, Canedy CL, Kim CS, Kim M, Merritt CD, Abell J, and Meyer JR 2013 Interband cascade lasers with low threshold powers and high output powers *IEEE J. Select. Top. Quantum Electron.* **19** 1200210

[29] Bauer A, Dallner M, Kamp M, Höfling S, Worschech L, and Forchel A 2010 Shortened injector interband cascade lasers for 3.3 to 3.6-μm emission *Opt. Engr.* **49** 111117

[30] Dallner M, Höfling S, and Kamp M 2013 Room-temperature operation of InAs-based interband-cascade-lasers beyond 6 μm *Electron. Lett.* **49** 286-287

[31] Tian ZB, Yang RQ, Mishima TD, Santos MB, and Johnson MB 2009 Plasmon-waveguide interband cascade lasers near 7.5 μm *IEEE Photon. Technol. Lett.* **21** 1588-1590

[32] Tian Z, Li L, Ye H, Yang RQ, Mishima TD, Santos MB, and Johnson MB 2012 InAs-based interband cascade lasers with emission wavelength at 10.4 μm *Electron. Lett.* **48** 113-114

[33] Olafsen LJ, Vurgaftman I, and Meyer JR 2004 Antimonide Mid-IR Lasers, Chap. 3 in *Long-Wavelength Infrared Semiconductor Lasers*, ed. H. K. Choi (John Wiley & Sons, Hoboken)

[34] Yang RQ 2013 Interband Cascade Lasers, Chap. 12 in *Semiconductor lasers: fundamentals and applications*, edited by A. Baranov and E. Tournie, Woodhead Publishing Limited, Cambridge, UK

[35] Yang RQ and Pei SS 1996 Novel type-II quantum cascade lasers J. Appl. Phys. **79**, 8197-8203

[36] Olesberg JT and Flatte ME 2006 Theory of mid-wavelength infrared laser active regions: intrinsic properties and design strategies, , Chap. 1 in *Mid-infrared Semiconductor Optoelectronics* ed. A. Krier (Springer)

[37] Getty JT, Skogen EJ, Johansson LA, and Coldren LA 2003 CW operation of 1.55-μm bipolar cascade laser with record differential efficiency, low threshold, and 50 O matching *IEEE Photon. Technol. Lett.* **15** 1513-1515

[38] Weih R, Bauer A, Kamp M, and Höfling S 2013 Interband cascade lasers with AlGaAsSb bulk cladding layers. *Opt. Mater. Expr.* **3** 1624-1631

[39] Bewley WW, Lindle JR, Canedy CL, Kim M, Kim CS, Larrabee DC, Vurgaftman I, and Meyer JR 2008 Gain, loss, and internal efficiency in interband cascade lasers emitting at λ = 3.6-4.1 μm *J. Appl. Phys.* **103** 013114

[40] Chandolo A, Pino R, and Dutta PS, 2005 Below bandgap optical absorption in tellurium-doped GaSb *Semicond. Sci. Technol.* **20** 886-893

[41] Bewley WW, Canedy CL, Kim CS, Vurgaftman I, Kim M, and Meyer JR 2004 Antimonide type-II "W" lasers: Growth studies and guided-mode leakage into substrate *Physica E* **20** 466-470

[42] Leavitt RP, Bruno JD, Bradshaw JL, Lascola KM, Pham JT, Towner FJ, Suchalkin S, Belenky G, Vurgaftman I, Canedy CL, Bewley WW, Kim CS, Kim M, Merritt CD, Meyer JR 2012 High performance interband cascade lasers at 3.8 microns *Proc. of SPIE* **8277** 82771E

[43] Tuttle G, Kroemer H, English JH 1990 Effects of interface layer sequencing on the transport properties of InAs/AlSb quantum wells: Evidence for antisite donors at the InAs/AlSb interface *J. Appl. Phys.* **67** 3032–7

[44] Spitzer J, Hijpner A, Kuball M, Cardona M, Jenichen J, Neuroth H, Brar , Kroemer H 1995 Influence of the interface composition of InAs/AlSb superlattices on their optical and structural properties *J. Appl. Phys.* **77** 811–20

[45] Jenichen B, Stepanov SA, Brar B, Kroemer H 1995 Interface roughness of InAs/AlSb superlattices investigated by x-ray scattering *J. Appl. Phys.* **79** 120

[46] Bauer A, Dallner M, Herrmann A, Lehnhardt T, Kamp M, Höfling S, Worschech L, Forchel A 2010 Atomic scale interface engineering for strain compensated epitaxially grown InAs/AlSb superlattices *Nanotechnology* **21** 455603

[47] Koerperick EJ, Murray LM, Norton DT, Boggess TF, Prineas JP 2010 Optimization of MBE-grown GaSb buffer layers and surface effects of antimony stabilization flux *J. of Crystal Growth* **312** 185 - 191

[48] Yang MJ, Moore WJ, Bennett BR, Shanabrook BV, Cross JO, Bewley WW, Felix CL, Vurgaftman I, Meyer JR 1999 Optimum growth parameters for type-II infrared lasers *J. Appl. Phys.* 86 1796

[49] Yang MJ, Moore WJ, Bennett BR, Shanabrook BV, Cross JO, Bewley WW, Felix CL, Vurgaftman I, Meyer JR 1999 Optimum growth parameters for type-II infrared lasers *J. Appl. Phys.* **86** 1796

[50] Canedy CL, Boishin GI, Bewley WW, Kim CS, Vurgaftman I , Kim M, Lindle JR, Meyer JR, Whitman LJ 2004 Correlating growth conditions with photoluminescence and lasing properties of mid-IR antimonide type II ''W'' structures *J. Vac. Sci. Technol.* B **22** 1575

[51] Canedy CL, Bewley WW, Boishin GI, Kim CS, Vurgaftman I, Kim M, Meyer JR, Whitman LJ 2005 Molecular beam epitaxy growth and characterization of mid-IR type-II "W" diode lasers *J. Vac. Sci. Technol.* B **23** 1119

[52] Canedy CL, Abell J, Bewley WW, Aifer EH, Kim CS, Nolde JA, Kim M, Tischler JG, Lindle JR, Jackson EM, Vurgaftman I, Meyer JR 2010 Molecular beam epitaxial growth effects on type-II antimonide lasers and photodiodes *J. Vac. Sci. Technol.* B **28** C3G8

[53] Janiak F, Motyka M, Sek G, Dyksik M, Ryczko K, Misiewicz J, Weih R, Höfling S, Kamp M, Patriarche G 2013 Effect of arsenic on the optical properties of GaSb-based type II quantum wells with quaternary GaInAsSb layers *J. Appl. Phys.* **114** 223510

[54] Forouhar S, Borgentun C, Frez C, Briggs RM, Bagheri M, Canedy CL, Kim CS, Kim M, Bewley WW, Merritt CD, Abell J, Vurgaftman I, and Meyer JR 2014 Reliable mid-infrared laterally-coupled distributed-feedback interband cascade lasers *Appl. Phys. Lett.* **105** 051110

[55] Canedy CL, Abell J, Merritt CD, Bewley WW, Kim CS, Vurgaftman I, Meyer JR, and Kim M 2014 Pulsed and CW Performance of 7-Stage Interband Cascade Lasers *Opt. Expr.* **22** 7702

[56] Canedy CL, Abell J, Merritt CD, Bewley WW, Kim CS, Kim M, Vurgaftman I, Meyer JR 2014 High-Power CW Performance of 7-Stage Interband Cascade Lasers *Proc. SPIE* **9002** 90021C

[57] Zhou C, Vurgaftman I, Canedy CL, Kim CS, Kim M, Bewley WW, Merritt CD, Abell J, Meyer JR, Hoang A, Haddadi A, Razeghi M, Grayson M 2013 Thermal conductivity tensors of the cladding and active layers of antimonide infrared lasers and detectors *Optical Materials Express* **3** 1632

[58] Bradshaw JL, Breznay NP, Bruno JD, Gomes JM, Pham JT, Towner FJ, Wortman DE, Tober RL, Monroy CJ, Olver KA 2004 Recent progress in the development of type II interband cascade lasers *Physica E* **20** 479 – 485

[59] Bewley WW, Kim CS¸ Kim M¸ Merritt CD, Canedy CL, Vurgaftman I, Abell J, Meyer JR 2012 Epitaxial-side-down-mounted interband cascade lasers *23rd IEEE Int. Semicond. Laser Conf.* 26-27

[60] Bauer A, Rößner K, Lehnhardt T, Kamp M, Höfling S, Worschech L, Forchel A 2011 Mid-infrared semiconductor heterostructure lasers for gas sensing applications *Semicond. Sci. Technol*. **26** 014032

[61] Kim CS, Kim M, Abell J, Bewley WW, Merritt CD, Canedy CL, Vurgaftman I, Meyer JR 2012 Mid-infrared distributed-feedback interband cascade lasers with continuous-wave single-mode emission to 80°C *Appl. Phys. Lett.* **101** 061104

[62] Weih R, Nähle L, Höfling S, Koeth J, Kamp M 2014 Single mode interband cascade lasers based on lateral metal gratings *Appl. Phys. Lett.* **105** 071111

[63] Bewley WW, Canedy CL, Kim CS, Kim M, Merritt CD, Abell J, Vurgaftman I, Meyer JR 2012 Continuous-wave interband cascade lasers operating above room temperature at λ = 4.7-5.6 µm *Opt. Expr.* **20** 3235-3240

[64] Weih R, Kamp M, Höfling S 2013 Interband cascade lasers with room temperature threshold current densities below 100 A/cm^2 *Appl. Phys.Lett.* **102** 231123

[65] Bauer A, Langer F, Dallner M, Kamp M, Motyka M, Sek G, Ryczko K, Misiewicz J, Höfling S, Forchel A 2009 Emission wavelength tuning of interband cascade lasers in the 3-4 µm spectral range *Appl. Phys. Lett.* **95** 251103

[66] Bewley WW, Canedy CL, Kim CS, Kim M, Merritt CD, Abell J, Vurgaftman I, Meyer JR 2012 High-power room-temperature continuous-wave mid-infrared interband cascade lasers *Opt. Expr.* **20** 20894-20901

[67] Bai Y, Bandyopadhyay N, Tsao S, Selcuk E, Slivken S, Razeghi M 2010 Highly temperature insensitive quantum cascade lasers *Appl. Phys. Lett.* **97** 251104

[68] Meyer JR, Vurgaftman I, Canedy CL, Abell J, Kim M, Kim CS, Merritt CD, and Bewley WW 2014 The Interband Cascade Laser – Competing with or Complementary to the QCL? *Int. Quantum Cascade Laser School and Workshop* (7-12 September 2014, Policoro Italy)

[69] Bewley WW, Lindle JR, Kim CS, Vurgaftman I, Meyer JR, Evans AJ, Yu JS, Slivken S, and Razeghi M 2005 Beam steering in high-power CW quantum cascade lasers IEEE J. Quantum Electron. **41** 833
[70] Walpole JN, Kintzer ES, Chinn SR, Wang CA, Missaggia LJ 1992 High power strained layer InGaAs/AlGaAs tapered traveling wave amplifier *Appl. Phys. Lett.* **61** 740
[71] Walpole JN 1996 Semiconductor amplifiers and lasers with tapered gain regions *Opt. Quant. Electron.* **28** 623
[72] Bewley WW, Kim CS, Canedy CL, Merritt CD, Vurgaftman I, Abell J, Meyer JR, Kim M 2013 High-power, high-brightness continuous-wave interband cascade lasers with tapered ridges *Appl. Phys. Lett.* **103** 111111
[73] Kim CS, Kim M, Bewley WW, Lindle JR, Canedy CL, Nolde JA, Larrabee DC, Vurgaftman I, Meyer JR 2008 Broad-stripe, single-mode, mid-IR interband cascade laser with photonic-crystal distributed-feedback grating *Appl. Phys. Lett.* **92** 071110
[74] Kim CS, Kim M, Bewley WW, Lindle JR, Canedy CL, Abell J, Vurgaftman I, Meyer JR 2009 Corrugated-sidewall interband cascade lasers with single-mode midwave-infrared emission at room temperature *Appl. Phys. Lett.* **95** 231103
[75] Edlinger MV, Scheuermann J, Weih R, Zimmermann C, Nähle L, Fischer M, Koeth J, Höfling S, Kamp M 2014 Monomode Interband Cascade Lasers at 5.2 µm for Nitric Oxide Sensing *Phot.Tec. Lett.* **26** 480
[76] Kim CS, Kim M, Bewley WW, Canedy CL, Lindle JR, Vurgaftman I, Meyer JR 2007 High-Power Single-Mode Distributed-Feedback Interband Cascade Lasers for the Midwave-Infrared *Phot. Tech. Lett.* **19** 158
[77] Kim CS, Kim M, Abell J, Bewley WW, Merritt CD, Canedy CL, Vurgaftman I, Meyer JR 2012 Mid-infrared distributed-feedback interband cascade lasers with continuous-wave single-mode emission to 80°C *Appl. Phys. Lett.* **101** 061104
[78] Weih R, Nähle L, Höfling S, Koeth J, Kamp M 2014 Single mode interband cascade lasers based on lateral metal gratings *Appl. Phys. Lett.* **105** 071111
[79] Vurgaftman I, Meyer JR, Canedy CL, Bewley WW, Kim CS, Kim M, and Merritt CD 2009 (Filed) Interband cascade lasers with engineered carrier densities U.S. Patent #8,798,111
[80] Kurtz SR, Allerman AA, Biefeld RM, and Baucom KC, 1998 Cascaded midinfrared lasers with type I InAsSb quantum wells *Appl. Phys. Lett.* **72** 2093-2095
[81] L.Shterengas, R.Liang, G.Kipshidze, T.Hosoda, S.Suchalkin, G.Belenky 2013 Type-I quantum well cascade diode lasers emitting near 3 µm *Appl. Phys. Lett.* **103** 121108
[82] Gmachl C, Sivco D L, Colombelli R, Capasso F, Cho A 2002 Ultra-broadband semiconductor laser *Nature* **415** 883;
[83] Wittmann A.; Hugi A.; Gini E; Hoyler N, Faist J 2008 Heterogeneous High-Performance Quantum-Cascade Laser Sources for Broad-Band Tuning *IEEE Journal of Quantum Electronics* **44** 1083
[84] Jiang Y, Li L, Tian Z, Ye H, Zhao L, Yang R Q, Mishima T D, Santos M B, Johnson M B, Mansour K 2014 Electrically widely tunable interband cascade lasers *J. Appl. Phys.* **115** 113101
[85] Li L, Zhao L, Jiang Y, Yang RQ, Keay JC, Mishima TD, Santos MB, and Johnson MB 2012 Single-waveguide dual-wavelength interband cascade lasers *Appl. Phys. Lett.* **101** 171118
[86] Straub A, Gmachl C, Sivco D L, Sergent A. M., Capasso F, Cho A Y, 2002 Simultaneously two wavelength (5.0 and 7.5 µm) single mode and tunable quantum cascade distributed feedback laser *Electron. Lett.* **38** 565
[87] Höfling S, Seufert J, Fischer M, Rösener B, Reithmaier J P , Forchel A 2006 Mode Switching and Single Mode Tuning in Two Segment Distributed Feedback Quantum Cascade Lasers *Electron. Lett.* **42** 220
[88] Lee B G, Zhang H A Pflügl C, Diehl L, Belkin M A, Fischer M, Wittmann A, Faist J, Capasso F 2009 Broadband Distributed-Feedback Quantum Cascade Laser Array Operating from 8.0 to 9.8µm *IEEE Phot. Technol. Lett.* **21** 914
[89] Lee B G, Zhang H A Pflügl C, Diehl L, Belkin M A, Fischer M, Wittmann A, Faist J, Capasso F 2009 Broadband Distributed-Feedback Quantum Cascade Laser Array Operating from 8.0 to 9.8µm *IEEE Phot. Technol. Lett.* **21** 914
[87] Höfling S, Heinrich J, Reithmaier J P, Forchel A, Seufert J, Fischer M, Koeth J 2006 Widely tunable single-mode quantum cascade lasers with two monolithically coupled Fabry-Perot cavities *Appl. Phys. Lett.* **89** 241126
[91] Slivken S, Bandyopadhyay N, Tsao S, Nida S, Bai Y, Lu Q Y, Razeghi M 2012 Sampled grating, distributed feedback quantum cascade lasers with broad tunability and continuous operation at room temperature *Appl. Phys. Lett.* **100** 261112
[92] Li J V, Yang R Q, Hill C J, Chuang S L 2005 Interband cascade detectors with room temperature photovoltaic operation *Appl. Phys. Lett.* **86** 101102

[93] Schwarz B, Reininger P, Detz H, Zederbauer T, Andrews A M, Schrenk W, Strasser G 2013 Interband cascade detectors with room temperature photovoltaic operation *Sensors* **13**, 2196

[94] Arafin S, Bachmann A, Shirazi KK, Amann MC 2009 Electrically pumped continuous-wave vertical-cavity surface-emitting lasers at 2.6μm *Appl. Phys. Lett.* **95** 131120

[95] Abell J, Kim CS, Bewley WW, Merritt CD, Canedy CL, Vurgaftman I, Meyer JR, and Kim M 2014 Mid-infrared interband cascade light emitting devices with milliwatt output powers at room temperature *Appl. Phys. Lett.* **104** 261103-261106